

A Convex Geodesic Selective Model for Image Segmentation

MICHAEL ROBERTS^{†*}, KE CHEN^{††} AND KLAUS L. IRION[‡]

[†]Centre for Mathematical Imaging Techniques and
Department of Mathematical Sciences,
University of Liverpool, United Kingdom

[‡]Department of Radiology, Manchester University NHS Foundation Trust, Manchester, UK

Abstract

Selective segmentation is an important application of image processing. In contrast to global segmentation in which all objects are segmented, selective segmentation is used to isolate specific objects in an image and is of particular interest in medical imaging – permitting segmentation and review of a single organ. An important consideration is to minimise the amount of user input to obtain the segmentation; this differs from interactive segmentation in which more user input is allowed than selective segmentation. To achieve selection, we propose a selective segmentation model which uses the edge-weighted geodesic distance from a marker set as a penalty term. It is demonstrated that this edge-weighted geodesic penalty term improves on previous selective penalty terms. A convex formulation of the model is also presented, allowing arbitrary initialisation. It is shown that the proposed model is less parameter dependent and requires less user input than previous models. Further modifications are made to the edge-weighted geodesic distance term to ensure segmentation robustness to noise and blur. We can show that the overall Euler-Lagrange equation admits a unique viscosity solution. Numerical results show that the result is robust to user input and permits selective segmentations that are not possible with other models.

Keywords. Variational model, partial differential equations, image segmentation, additive operator splitting, viscosity solution, geodesic.

1. INTRODUCTION

Segmentation of an image into its individual objects is one incredibly important application of image processing techniques. Segmentation can take two forms; firstly global segmentation for isolation of all foreground objects in an image from the background and secondly, selective segmentation for isolation of a subset of the objects in an image from the background. A comprehensive review of selective segmentation can be found in [7, 19] and in [45] for medical image segmentation where selection refers to extraction of single organs.

Approaches to image segmentation broadly fall into two classes; region-based and edge-based. Some region-based approaches are region growing [1], watershed algorithms [40], Mumford-Shah [29] and Chan-Vese [11]. The final two of these are partial differential equations (PDEs)-based variational approaches to the problem of segmentation. There are also models which

*The first author wishes to thank the UK EPSRC and the Liverpool Heart and Chest Hospital for supporting the work through an iCASE PhD award.

[†]Email k.chen@liverpool.ac.uk, Web: www.liv.ac.uk/cmit (Corresponding author). Work supported by UK EPSRC grant EP/N014499/1.

30 mix the two classes to use the benefits of the region-based and edge-based approaches and will
31 incorporate features of each. Edge-based methods aim to encourage an evolving contour towards
32 the edges in an image and normally require an edge detector function [8]. The first edge-based
33 variational approach was devised by Kass et al. [22] with the famous snakes model, this was
34 further developed by Casselles et al. [8] who introduced the Geodesic Active Contour (GAC)
35 model. Region-based global segmentation models include the well known works of Mumford-
36 Shah [29] and Chan-Vese [11]. Importantly they are non-convex and hence a minimiser of these
37 models may only be a local, not the global, minimum. Further work by Chan et al. [10] gave rise
38 to a method to find the global minimiser for the Chan-Vese model under certain conditions.

39 This paper is mainly concerned with selective segmentation of objects in an image, given a set of
40 points near the object or objects to be segmented. It builds in such user input to a model using a
41 set $\mathcal{M} = \{(x_i, y_i) \in \Omega, 1 \leq i \leq k\}$ where $\Omega \subset \mathbb{R}^2$ is the image domain [4, 5, 17]. Nguyen et al.
42 [30] considered marker sets \mathcal{M} and \mathcal{A} which consist of points inside and outside, respectively,
43 the object or objects to be segmented. Gout et al. [17] combined the GAC approach with the
44 geometrical constraint that the contour passes through the points of \mathcal{M} . This was enforced
45 with a distance function which is zero at \mathcal{M} and non-zero elsewhere. Badshah and Chen [4]
46 then combined the Gout et al. model with [11] to incorporate a constraint on the intensity in
47 the selected region, thereby encouraging the contour to segment homogeneous regions. Rada
48 and Chen [36] introduced a selective segmentation method based on two-level sets which was
49 shown to be more robust than the Badshah-Chen model. We also refer to [5, 23] for selective
50 segmentation models which include different fitting constraints, using coefficient of variation
51 and the centroid of \mathcal{M} respectively. None of these models have a restriction on the size of
52 the object or objects to be detected and depending on the initialisation these methods have the
53 potential to detect more or fewer objects than the user desired. To address this and to improve
54 on [36], Rada and Chen [37] introduced a model combining the Badshah-Chen [4] model with a
55 constraint on the area of the objects to be segmented. The reference area used to constrain the
56 area within the contour is that of the polygon formed by the markers in \mathcal{M} . Spencer and Chen
57 [39] introduced a model with the distance fitting penalty as a standalone term in the energy
58 functional, unbounding it from the edge detector term of the Gout et al. model.

59 All of the above selective segmentation models discussed are non-convex and hence the final
60 result depends on the initialisation. Spencer and Chen [39], in the same paper, reformulated
61 the model they introduced to a convex form using convex relaxation and an exact penalty term
62 as in [10]. Their model uses Euclidean distance from the marker set \mathcal{M} as a distance penalty
63 term, however we propose replacing this with the edge-weighted geodesic distance from \mathcal{M} (we
64 call this simply the geodesic distance). This distance increases at edges in the image and is more
65 intuitive for selective segmentation. The proposed model is given as a convex relaxed model with
66 exact penalty term and we give a general existence and uniqueness proof for the viscosity solution
67 to the PDE given by its Euler-Lagrange equation, which is also applicable to a whole class of PDEs
68 arising in image segmentation. We note that the use of geodesic distance for segmentation has
69 been considered before [6, 34], however the models only use geodesic distance as the fitting term
70 within the regulariser, so are liable to make segmentation errors for poor initialisation or complex
71 images. Here we take a different approach, by including geodesic distance as a standalone fitting
72 term, separate from the regulariser, and using intensity fitting terms to ensure robustness.

73 In this paper we only consider 2D images, however for completion we remark that 3D seg-
74 mentation models do exist [25, 44] and it is simple to extend the proposed model to 3D. The
75 contributions of this paper can be summarised as follows:

-
- 76 • We incorporate the geodesic distance as a distance penalty term within the variational
77 framework.
 - 78 • We propose a convex selective segmentation model using this penalty term and demonstrate
79 how it can achieve results which cannot be achieved by other models.
 - 80 • We improve the geodesic penalty term, focussing on improving robustness to noise and
81 improving segmentation when object edges are blurred.
 - 82 • We give an existence and uniqueness proof for the viscosity solution for the PDEs associated
83 with a whole class of segmentation models (both global and selective).

84 We find that the proposed model gives accurate segmentation results for a wide range of param-
85 eters and, in particular, when segmenting the same objects from the same modality images, i.e.
86 segmenting lungs from CT scans, the parameters are very similar from one image to the next
87 to obtain accurate results. Therefore, this model may be used to assist the preparation of large
88 training sets for deep learning studies [32, 41, 42] that concern segmentation of particular objects
89 from images.

90 The paper is structured as follows; in §2 we review some global and selective segmentation
91 models. In §3 we discuss the geodesic distance penalty term, propose a new convex model and
92 also address weaknesses in the naïve implementation of the geodesic distance term. In §4 we
93 discuss the non-standard AOS scheme, introduced in [39], which we use to solve the model.
94 In §5 we give an existence and uniqueness proof for a general class of PDEs arising in image
95 segmentation, thereby showing that for a given initialisation the solution to our model is unique.
96 In §6 we compare the results of the proposed model to other selective segmentation models, show
97 that the proposed model is less parameter dependent than other models and is more robust to
98 user input. Finally, in §7 we provide some concluding remarks.

99 2. REVIEW OF VARIATIONAL SEGMENTATION MODELS

100 Although we focus on selective segmentation, it is illuminating to introduce some global segmen-
101 tation models first. Throughout this paper we denote the original image by $z(x, y)$ with image
102 domain $\Omega \subset \mathbb{R}^2$.

103 2.1. Global Segmentation

104 The model of Mumford and Shah [29] is one of the most famous and important variational
105 models in image segmentation. We will review its two-dimensional piecewise constant variant,
106 commonly known as the Chan-Vese model [11], which takes the form

$$107 F_{CV}(\Gamma, c_1, c_2) = \mu \cdot \text{length}(\Gamma) + \lambda_1 \int_{\Omega_1} |z(x, y) - c_1|^2 d\Omega + \lambda_2 \int_{\Omega_2} |z(x, y) - c_2|^2 d\Omega \quad (1)$$

108 where the foreground Ω_1 is the subdomain to be segmented, the background $\Omega_2 = \Omega \setminus \Omega_1$ and
109 $\mu, \lambda_1, \lambda_2$ are fixed non-negative parameters. The values c_1 and c_2 are the average intensities of
110 $z(x, y)$ inside Ω_1 and Ω_2 respectively. We use a level set function

$$111 \phi(x, y) = \begin{cases} > 0, & (x, y) \in \Omega_1, \\ 0, & (x, y) \in \Gamma, \\ < 0, & \text{otherwise,} \end{cases}$$

1
2
3
4
5
6 110 to track $\Gamma = \{(x, y) \in \Omega \mid \phi(x, y) = 0\}$ (an idea popularised by Osher and Sethian [31]) and
7 reformulate (1) as
8

$$9 \quad F_{CV}(\phi, c_1, c_2) = \mu \int_{\Omega} |\nabla H_{\varepsilon}(\phi)| \, d\Omega + \lambda_1 \int_{\Omega} (z(x, y) - c_1)^2 H_{\varepsilon}(\phi) \, d\Omega \quad (2)$$

$$11 \quad + \lambda_2 \int_{\Omega} (z(x, y) - c_2)^2 (1 - H_{\varepsilon}(\phi)) \, d\Omega,$$

12
13
14
15 112 with $H_{\varepsilon}(\phi)$ a smoothed Heaviside function such as $H_{\varepsilon}(\phi) = \frac{1}{2} + \frac{1}{\pi} \arctan(\frac{\phi}{\varepsilon})$ for some ε , we set
16 113 $\varepsilon = 1$ throughout. We solve this in two stages, first with ϕ fixed we minimise F_{CV} with respect to
17 114 c_1 and c_2 , obtaining

$$19 \quad c_1 = \frac{\int_{\Omega} H_{\varepsilon}(\phi) \cdot z(x, y) \, d\Omega}{\int_{\Omega} H_{\varepsilon}(\phi) \, d\Omega}, \quad c_2 = \frac{\int_{\Omega} (1 - H_{\varepsilon}(\phi)) \cdot z(x, y) \, d\Omega}{\int_{\Omega} (1 - H_{\varepsilon}(\phi)) \, d\Omega}, \quad (3)$$

20
21
22
23 115 and secondly, with c_1 and c_2 fixed we minimise (2) with respect to ϕ . This requires the calculation
24 116 of the associated Euler-Lagrange equations. A drawback of the Chan-Vese energy functional (2)
25 117 is that it is non-convex. Therefore a minimiser may only be a local minimum and not the global
26 118 minimum and the final segmentation result is dependent on the initialisation. Chan et al. [10]
27 119 reformulated (2) using an exact penalty term to obtain an equivalent convex model – we use this
28 120 same technique in §2.2 for the Geodesic Model.

31 2.2. Selective Segmentation

32
33 122 Selective segmentation models make use of user input, i.e. a marker set \mathcal{M} of points near the
34 123 object or objects to be segmented. Let $\mathcal{M} = \{(x_i, y_i) \in \Omega, 1 \leq i \leq k\}$ be such a marker set. The
35 124 aim of selective segmentation is to design an energy functional where the segmentation contour
36 125 Γ is close to the points of \mathcal{M} .

37
38
39 126 **Early work.** An early model by Caselles et al. [8], commonly known as the Geodesic Active
40 127 Contour (GAC) model, uses an edge detector function to ensure the contour follows edges, the
41 128 functional to minimise is given by

$$42 \quad \int_{\Gamma} g(|\nabla z(x, y)|) \, d\Gamma.$$

43
44
45
46 129 The term $g(|\nabla z(x, y)|)$ is an edge detector, one example is $g(s) = 1/(1 + \beta s^2)$ with β a tuning
47 130 parameter. It is common to smooth the image with a Gaussian filter G_{σ} where σ is the kernel
48 131 size, i.e. use $g(|\nabla (G_{\sigma} * z(x, y))|)$ as the edge detector. This mitigates the effect of noise in the
49 132 image, giving a more accurate edge detector. Gout et al. [25] built upon the GAC model by
50 133 incorporating a distance term $\mathcal{D}(x, y)$ into this integral, i.e. the integrand is $\mathcal{D}(x, y)g(|\nabla z|)$. The
51 134 distance term is a penalty on the distance from \mathcal{M} , this model encourages the contour to be
52 135 near to the set \mathcal{M} whilst also lying on edges. However this model struggles when boundaries
53 136 between objects and their background are fuzzy or blurred. To address this, Badshah and Chen
54 137 [4] introduced a new model which adds the intensity fitting terms from the Chan-Vese model (1)
55 138 to the Gout et al. model. However, their model has poor robustness [36]. To improve on this,
56 139 Rada and Chen [37] introduced a model which adds an area fitting term into the Badshah-Chen
57 140 model and is far more robust.

1
2
3
4
5
6
7
8
9
10
11
12
13
14
15
16
17
18
19
20
21
22
23
24
25
26
27
28
29
30
31
32
33
34
35
36
37
38
39
40
41
42
43
44
45
46
47
48
49
50
51
52
53
54
55
56
57
58
59
60
61
62
63
64
65

141 **The Rada-Chen model** [37]. We first briefly introduce this model, defined by

$$\begin{aligned}
F_{RC}(\phi, c_1, c_2) = & \mu \int_{\Omega} \mathcal{D}(x, y) g(|\nabla z(x, y)|) |\nabla H_{\varepsilon}(\phi)| \, d\Omega \\
& + \lambda_1 \int_{\Omega} (z(x, y) - c_1)^2 H_{\varepsilon}(\phi) \, d\Omega + \lambda_2 \int_{\Omega} (z(x, y) - c_2)^2 (1 - H_{\varepsilon}(\phi)) \, d\Omega \quad (4) \\
& + \gamma \left[\left(\int_{\Omega} H_{\varepsilon}(\phi) \, d\Omega - A_1 \right)^2 + \left(\int_{\Omega} (1 - H_{\varepsilon}(\phi)) \, d\Omega - A_2 \right)^2 \right],
\end{aligned}$$

142 where $\mu, \lambda_1, \lambda_2, \gamma$ are fixed non-negative parameters. There is freedom in choosing the distance
143 term $\mathcal{D}(x, y)$, see [37] for some examples. A_1 is the area of the polygon formed from the points
144 of \mathcal{M} and $A_2 = |\Omega| - A_1$. The final term of this functional puts a penalty on the area inside a
145 contour being very different to A_1 . One drawback of the Rada-Chen model is that the selective
146 fitting term uses no location information from the marker set \mathcal{M} . Therefore the result can be
147 a contour which is separated over the domain into small parts, whose sum area totals the area
148 fitting term.

149 **Nguyen et al.** [30]. This model is based on the GAC model and uses likelihood functions as
150 fitting terms, it has the energy functional

$$\begin{aligned}
F_{NG}(\phi) = & \mu \int_{\Omega} g(|\nabla z(x, y)|) |\nabla H_{\varepsilon}(\phi)| \, d\Omega \\
& + \lambda \int_{\Omega} \alpha (P_B(x, y) - P_F(x, y)) + (1 - \alpha) (1 - 2P(x, y)) \phi \, d\Omega
\end{aligned}$$

151 where $P_B(x, y)$ and $P_F(x, y)$ are the normalised log-likelihoods that the pixel (x, y) is in the fore-
152 ground and background respectively. $P(x, y)$ is the probability that pixel (x, y) belongs to the
153 foreground, $\alpha \in [0, 1]$ and minimisation is constrained, requiring $\phi \in [0, 1]$, so $F_{NG}(\phi)$ is convex.
154 This model is good for many examples, see [30], however fails when the boundary of the object
155 to segment is non-smooth or has fine structures. Also, the final result is sometimes sensitive to
156 the marker sets used.

157 **The Spencer-Chen model** [39]. The authors introduced the following model

$$\begin{aligned}
F_{SC}(\phi, c_1, c_2) = & \mu \int_{\Omega} g(|\nabla z(x, y)|) |\nabla H_{\varepsilon}(\phi)| \, d\Omega + \lambda_1 \int_{\Omega} (z(x, y) - c_1)^2 H_{\varepsilon}(\phi) \, d\Omega \quad (5) \\
& + \lambda_2 \int_{\Omega} (z(x, y) - c_2)^2 (1 - H_{\varepsilon}(\phi)) \, d\Omega + \theta \int_{\Omega} \mathcal{D}_E(x, y) H_{\varepsilon}(\phi) \, d\Omega,
\end{aligned}$$

158 where $\mu, \lambda_1, \lambda_2, \theta$ are fixed non-negative parameters. Note that the regulariser of this model
159 differs from the Rada-Chen model (4) as the distance function $\mathcal{D}(x, y)$ has been separated from the
160 edge detector term and is now a standalone penalty term $\mathcal{D}_E(x, y)$. The authors use normalised
161 Euclidean distance $\mathcal{D}_E(x, y)$ from the marker set \mathcal{M} as their distance penalty term. We will
162 discuss this later in §3 as it is one of the key improvements we make to the Spencer-Chen model,
163 replacing the Euclidean distance term with a geodesic distance term.

164 **Convex Spencer-Chen model** [39]. Spencer and Chen use the ideas of [10] to reformulate (5)
165 into a convex minimisation problem. It can be shown that the Euler-Lagrange equations for
166 $F_{SC}(\phi, c_1, c_2)$ have the same stationary solutions as for

$$\begin{aligned}
F_{SC1}(u, c_1, c_2) = & \mu \int_{\Omega} g(|\nabla z(x, y)|) |\nabla u| \, d\Omega + \int_{\Omega} \left[\lambda_1 (z(x, y) - c_1)^2 - \lambda_2 (z(x, y) - c_2)^2 \right] u \, d\Omega \quad (6) \\
& + \theta \int_{\Omega} \mathcal{D}_E(x, y) u \, d\Omega,
\end{aligned}$$

1
2
3
4
5
6
167 with the minimisation constrained to $u \in [0, 1]$. This is a constrained convex minimisation which
7
168 can be reformulated to an unconstrained minimisation using an exact penalty term $v(u) :=$
8
169 $\max\{0, 2|u - \frac{1}{2}| - 1\}$ in the functional, which encourages the minimiser to be in the range $[0, 1]$.
9
170 In [39] the authors use a smooth approximation $v_\varepsilon(u)$ to $v(u)$ given by

$$v_\varepsilon(u) = H_\varepsilon \left(\sqrt{(2u - 1)^2 + \varepsilon} - 1 \right) \left[\sqrt{(2u - 1)^2 + \varepsilon} - 1 \right], \quad (7)$$

14
171 and perform the unconstrained minimisation of

$$F_{SC2}(u, c_1, c_2) = \mu \int_{\Omega} g(|\nabla z(x, y)|) |\nabla u| \, d\Omega + \int_{\Omega} \left[\lambda_1(z(x, y) - c_1)^2 - \lambda_2(z(x, y) - c_2)^2 \right] u \, d\Omega \quad (8)$$

$$+ \theta \int_{\Omega} \mathcal{D}_E(x, y) u \, d\Omega + \alpha \int_{\Omega} v_\varepsilon(u) \, d\Omega.$$

21
172 When $\alpha > \frac{1}{2} \| [\lambda_1(z(x, y) - c_1)^2 - \lambda_2(z(x, y) - c_2)^2] + \theta \mathcal{D}_E(x, y) \|_{L^\infty}$, the above functional has the
22
173 same set of stationary solutions as $F_{SC1}(u, c_1, c_2)$. It permits us to choose arbitrary u initialisation
23
174 to obtain the desired selective segmentation result due to its complexity.

25
175 **Convex Liu et al. model [26].** Recently, a convex model was introduced by Liu et al. which
26
176 applies a weighting to the data fitting terms, the functional to minimise is given by

$$F_{LIU}(u) = \mu \int_{\Omega} |\nabla u| \, d\Omega + \mu_2 \int_{\Omega} |\nabla u|^2 \, d\Omega + \lambda \int_{\Omega} \omega^2(x, y) |z - u|^2 \, d\Omega, \quad (9)$$

28
29
30
31
177 where μ, μ_2, λ are non-negative parameters and $\omega(x, y) = 1 - \mathcal{D}(x, y)g(|\nabla z|)$ where $\mathcal{D}(x, y)$ is a
178 distance function from marker set \mathcal{M} (see [26] for examples).

179 3. PROPOSED CONVEX GEODESIC SELECTIVE MODEL

34
35
36
180 We propose an improved selective model, based on the Spencer-Chen model, which uses geodesic
37
181 distance from the marker set \mathcal{M} as the distance term, rather than the Euclidean distance. Increasing
38
182 the distance when edges in the image are encountered gives a more accurate reflection of the
39
183 true similarity of pixels in an image from the marker set. We propose minimising the convex
40
184 functional

$$F_{CG}(u, c_1, c_2) = \mu \int_{\Omega} g(|\nabla z(x, y)|) |\nabla u| \, d\Omega + \int_{\Omega} \left[\lambda_1(z(x, y) - c_1)^2 - \lambda_2(z(x, y) - c_2)^2 \right] u \, d\Omega \quad (10)$$

$$+ \theta \int_{\Omega} \mathcal{D}_M(x, y) u \, d\Omega + \alpha \int_{\Omega} v_\varepsilon(u) \, d\Omega,$$

47
185 where $\mathcal{D}_M(x, y)$ is the edge-weighted geodesic distance from the marker set. In Figure 1, we
48
186 compare the normalised geodesic distance and the Euclidean distance from the same marker
49
187 point (i.e. set \mathcal{M} has one point in it); clearly the former gives a more intuitively correct distance
50
188 penalty than the latter. We will refer to this proposed model as the Geodesic Model.

53 3.1. Computing the Geodesic Distance Term $\mathcal{D}_M(x, y)$

54
55
190 The geodesic distance from the marker set \mathcal{M} is given by $\mathcal{D}_M(x, y) = 0$ for $(x, y) \in \mathcal{M}$ and
56
191 $\mathcal{D}_M(x, y) = \frac{\mathcal{D}_M^0(x, y)}{\| \mathcal{D}_M^0(x, y) \|_{L^\infty}}$ for $(x, y) \notin \mathcal{M}$, where $\mathcal{D}_M^0(x, y)$ is the solution of the following PDE

$$|\nabla \mathcal{D}_M^0(x, y)| = f(x, y), \quad \mathcal{D}_M^0(x_0, y_0) = 0, \quad (x_0, y_0) \in \mathcal{M}. \quad (11)$$

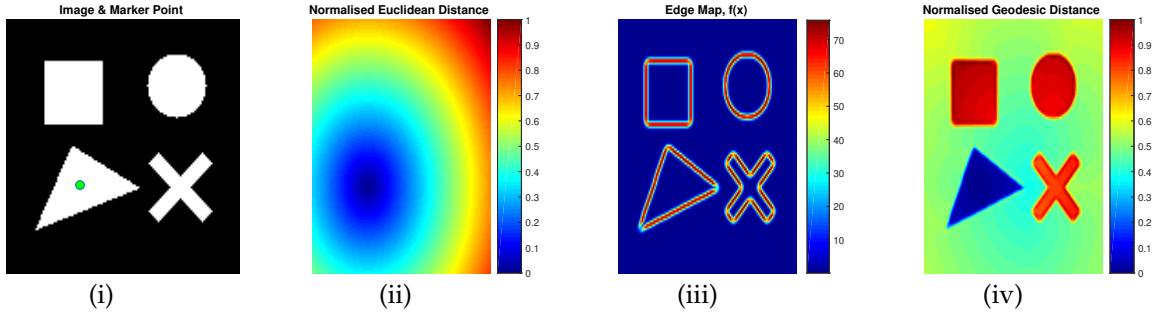


Figure 1: Comparison of distance measures. (i) Simple binary image with marker point; (ii) normalised Euclidean distance from marker point; (iii) edge map function $f(x)$ for the image; (iv) normalised geodesic distance from marker point.

where $f(x, y)$ is defined later on with respect to the image contents.

If $f(x, y) \equiv 1$ (i.e. $|\nabla \mathcal{D}_M^0(x, y)| = 1$) then the distance penalty $D_M(x, y)$ is simply the normalised Euclidean distance $\mathcal{D}_E(x, y)$ as used in the Spencer-Chen model (5). We have free rein to design $f(x, y)$ as we wish. Looking at the PDE in (11), we see that when $f(x, y)$ small this results in a small gradient in our distance function and it is almost flat. When $f(x, y)$ is large, we have a large gradient in our distance map. In the case of selective image segmentation, we want small gradients in homogeneous areas of the image and large gradients at edges. If we set

$$f(x, y) = \varepsilon_{\mathcal{D}} + \beta_G |\nabla z(x, y)|^2 \quad (12)$$

this gives us the desired property that in areas where $|\nabla z(x, y)| \approx 0$, the distance function increases by some small $\varepsilon_{\mathcal{D}}$; here image $z(x, y)$ is scaled to $[0, 1]$. At edges, $|\nabla z(x, y)|$ is large and the geodesic distance increases here. We set value of $\beta_G = 1000$ and $\varepsilon_{\mathcal{D}} = 10^{-3}$ throughout. In Figure 1, we see that the geodesic distance plot gives a low distance penalty on the triangle, which the marker indicates we would like segmented. There is a reasonable penalty on the background, and all other objects in the image have a very high distance penalty (as the geodesic to these points must cross two edges). This contrasts with the Euclidean distance, which gives a low distance penalty to some background pixels and maximum penalty to the pixels furthest away.

3.2. Comparing Euclidean and Geodesic Distance Terms

We briefly give some advantages of using the geodesic distance as a penalty term rather than Euclidean distance and a remark on the computational complexity for both distances.

1. **Parameter Robustness.** The Geodesic Model is more robust to the choice of the fitting parameter θ , as the penalty on the inside of the shape we want segmented is consistently small. It is only outside the shape where the penalty is large. Whereas with the Euclidean distance term we always have a penalty inside the shape we actually want to segment. This is due to the nature of the Euclidean distance which does not discriminate on intensity – this penalty can also be quite high if our marker set is small and doesn't cover the whole object.
2. **Robust to Marker Set Selection.** The geodesic distance term is far more robust to point selection, for example we can choose just one point inside the object we want to segment

and this will give a nearly identical geodesic distance compared to choosing many more points. This is not true of the Euclidean distance term which is very sensitive to point selection and requires markers to be spread in all areas of the object you want to segment (especially at extrema of the object).

Remark 1 (Computational Complexity). *The main concern of using the geodesic penalty term, which we obtain by solving PDE (11), would be that it takes a significant amount of time to compute compared to the Euclidean distance. However, using the fast marching algorithm of Sethian [38], the complexity of computing $\mathcal{D}_M(x, y)$ is $\mathcal{O}(N \log(N))$ for an image with N pixels. This is only marginally more complex than computing the Euclidean distance which has $\mathcal{O}(N)$ complexity [28].*

3.3. Improvements to Geodesic Distance Term

We now propose some modifications to the geodesic distance. Although the geodesic distance presents many advantages for selective image segmentation, we have three key disadvantages of this fitting term, which the Euclidean fitting term does not suffer.

1. **Not robust to noise.** The computation of the geodesic distance depends on $|\nabla z(x, y)|^2$ in $f(x, y)$ (see (11)). So, if an image contains a lot of noise, each noisy pixel appears as an edge and we get a misleading distance term.
2. **Objects far from \mathcal{M} with low penalty.** As the geodesic distance only uses marker set \mathcal{M} for its initial condition (see (11)), this can result in objects far from \mathcal{M} having a low distance penalty, which is clearly not desired.
3. **Blurred edges.** If we have two objects separated by a blurry edge and we have marker points only in one object, the geodesic distance will be low to the other object, as the edge penalty is weakly enforced for a blurry edge. We would desire low penalty inside the object with markers and a reasonable penalty in the joined object.

In Figure 2, each column shows an example for each of the problems listed above. We now propose solutions to each of these problems.

Problem 1: Noise Robustness. A naïve solution to the problem of noisy images would be to apply a Gaussian blur to $z(x, y)$ to remove the effect of the noise, so we change $f(x, y)$ to

$$\tilde{f}(x, y) = \varepsilon_D + \beta_G |\nabla G_\sigma * z(x, y)|^2 \quad (13)$$

where G_σ is a Gaussian convolution with standard deviation σ . However, the effect of Gaussian convolution is that it also blurs edges in the image. This then gives us the same issues described in Problem 3. We see in Figure 3 column 3, that the Gaussian convolution reduces the sharpness of edges and this results in the geodesic distance being very similar in adjacent objects – therefore we see more pixels with high geodesic distance. Our alternative to Gaussian blur is to consider anisotropic TV denoising. We refer the reader to [9, 33] for information on the model, here we just give the PDE which results from its minimisation:

$$\tilde{\mu} \nabla \cdot \left(g(|\nabla z(x, y)|) \frac{\nabla u}{|\nabla u|_{\varepsilon_2}} \right) + \iota(z(x, y) - u) = 0, \quad (14)$$

where $\tilde{\mu}, \iota$ are non-negative parameters (we fix throughout $\tilde{\mu} = 10^{-3}, \iota = 5 \times 10^{-4}$). It is proposed to apply a relatively small number of cheap fixed point Gauss-Seidel iterations (between 100 and

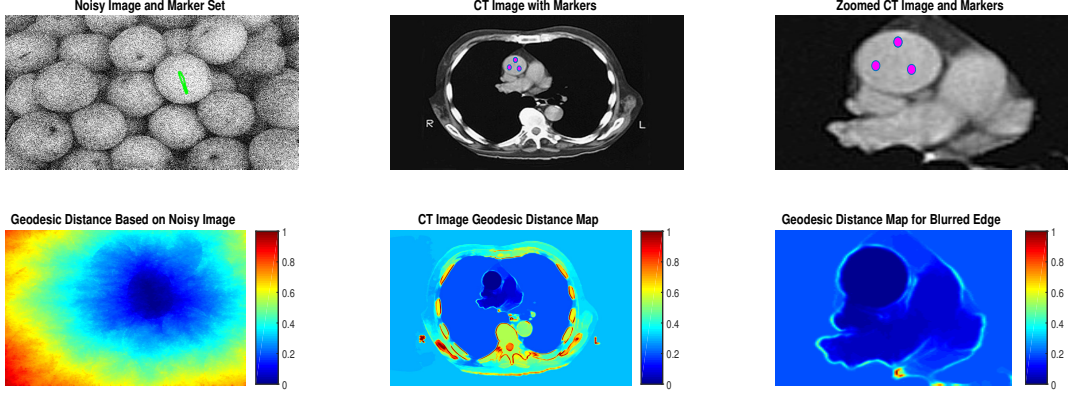


Figure 2: Examples of images showing the problems discussed and the resulting geodesic distance maps. Column 1 shows the lack of robustness to noise, column 2 shows that outside the patient we have unreasonably low distance penalty, column 3 shows how the blurred edge under the aorta leads to the distance term being very low throughout the heart.

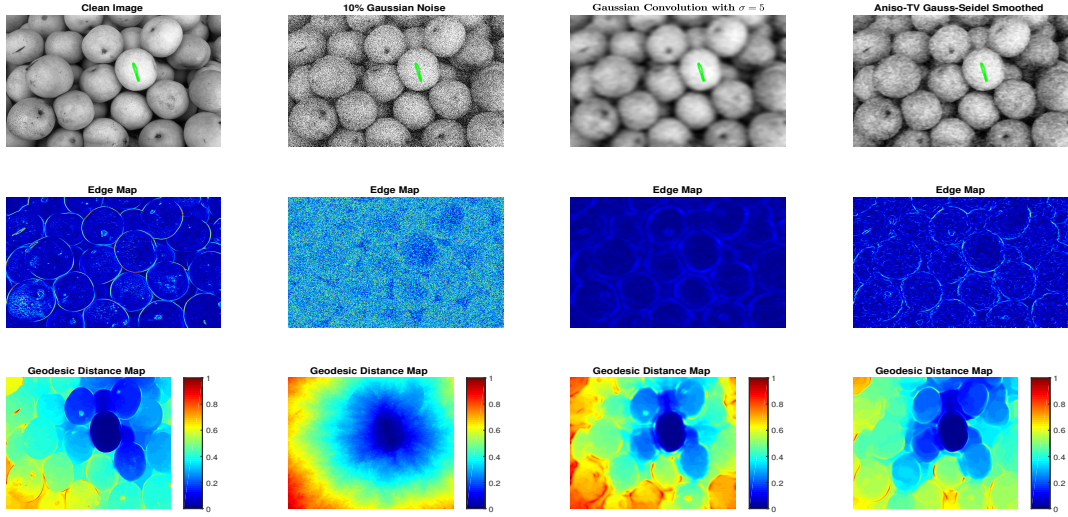


Figure 3: The edge maps and geodesic distance maps. (Left to right:) the clean image, the image with 10% Gaussian noise, the noisy image with Gaussian convolution applied ($\sigma = 5$) and for the noisy image with 100 iterations of anisotropic-TV Gauss-Seidel smoothing. The set \mathcal{M} is shown on the top row, it is the same for each image.

256 200) to the discretised PDE. We cycle through all pixels (i, j) and update $u_{i,j}$ as follows

$$u_{i,j} = \frac{A_{i,j}u_{i+1,j} + B_{i,j}u_{i-1,j} + C_{i,j}u_{i,j+1} + D_{i,j}u_{i,j-1}}{A_{i,j} + B_{i,j} + C_{i,j} + D_{i,j} + \iota} \quad (15)$$

257 where $A_{i,j} = \frac{\tilde{\mu}}{h_x^2} g(|\nabla z(x, y)|)_{i+1/2,j}$, $B_{i,j} = \frac{\tilde{\mu}}{h_x^2} g(|\nabla z(x, y)|)_{i-1/2,j}$, $C_{i,j} = \frac{\tilde{\mu}}{h_y^2} g(|\nabla z(x, y)|)_{i,j+1/2}$ and

258 $D_{i,j} = \frac{\tilde{\mu}}{\tilde{\mu}_y^2} g(|\nabla z(x,y)|)_{i,j-1/2}$. We update all pixels once per iteration and solve the PDE in (11)
 259 with $f(x,y)$ replaced by

$$f_1(x,y) = \varepsilon_{\mathcal{D}} + \beta_G |\nabla S^k(z(x,y))|^2 \quad (16)$$

260 where S represents the Gauss-Seidel iterative scheme and k is the number of iterations performed
 261 (we choose $k = 100$ in our tests). In the final column of Figure 3 we see that the geodesic distance
 262 map more closely resembles that of the clean image than the Gaussian blurred map in column
 263 3 and in Figure 4 we see that the segmentation results are qualitatively and quantitatively better
 using the anisotropic smoothing technique.

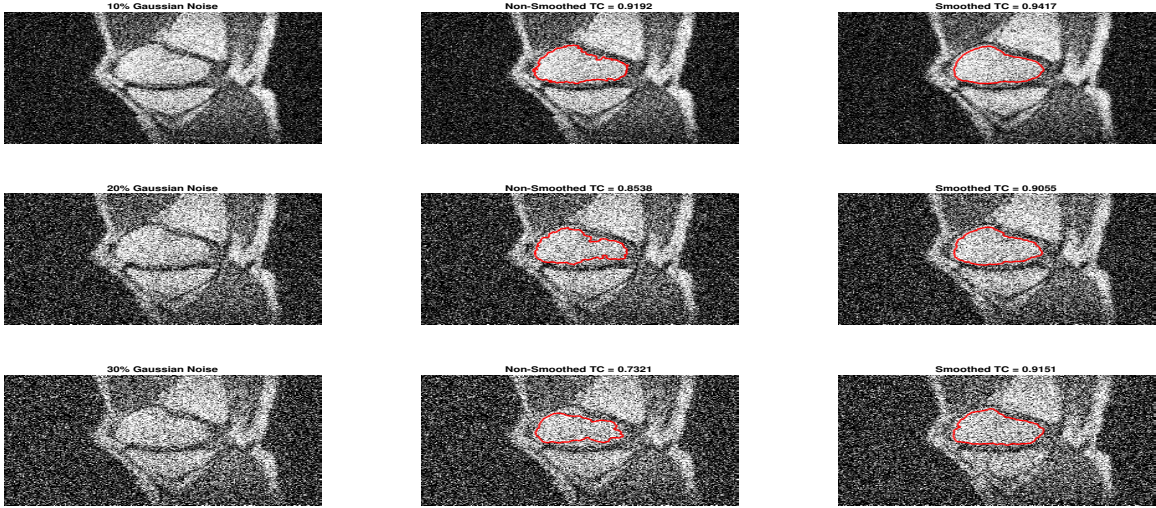


Figure 4: Segmentation results and Tanimoto Coefficients (see §6) for images with 10%, 20% and 30% Gaussian Noise with and without smoothing, $\lambda_1 = \lambda_2 = 5$, $\theta = 3$.

264
 265 **Problem 2: Objects far from \mathcal{M} with low penalty.**

266 In Figure 2 column 2 we see that the geodesic distance to the outside of the patient is lower than
 267 to their ribs. This is due to the fact that the region outside the body is homogeneous and there is
 268 almost zero distance penalty in this region. Similarly for Figure 3 column 4, the distances from
 269 the marker set to many surrounding objects is low, even though their Euclidean distance from
 270 the marker set is high. We wish to have the Euclidean distance $\mathcal{D}_E(x,y)$ incorporated somehow.
 271 Our solution is to modify the term $f_1(x,y)$ from (16) to

$$f_2(x,y) = \varepsilon_{\mathcal{D}} + \beta_G |\nabla S^k(z(x,y))|^2 + \vartheta \mathcal{D}_E(x,y). \quad (17)$$

272 In Figure 5 the effect of this is clear, as ϑ increases, the distance function resembles the Euclidean
 273 distance more. We use value $\vartheta = 10^{-1}$ in all experiments as it adds a reasonable penalty to pixels
 274 far from the marker set.

275 **Problem 3: Blurred edges.**

276 If there are blurred edges between objects in an image, the geodesic distance will not increase
 277 significantly at this edge. Therefore the final segmentation result is liable to include unwanted
 278 objects. We look to address this problem through the use of anti-markers. These are markers

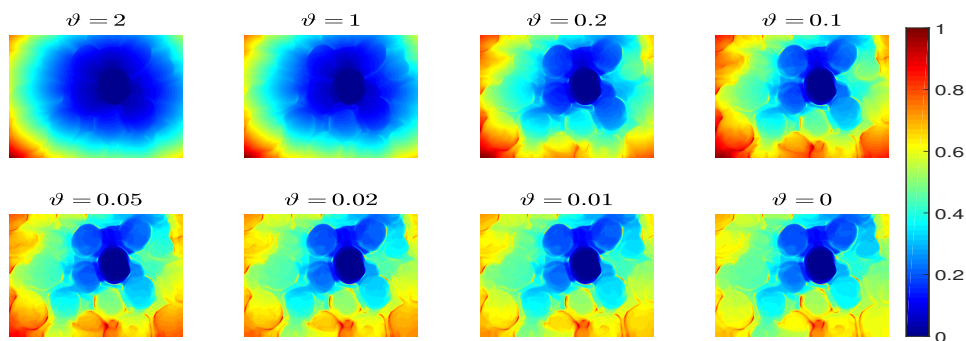


Figure 5: Displayed is $\mathcal{D}_M(x, y)$ using $f_2(x, y)$ for various ϑ values. The marker set is the same as that used in Figure 3.

279 which indicate objects that we do not want to segment, i.e. the opposite of marker points, we denote the set of anti-marker points by \mathcal{AM} . We propose to use a geodesic distance map from

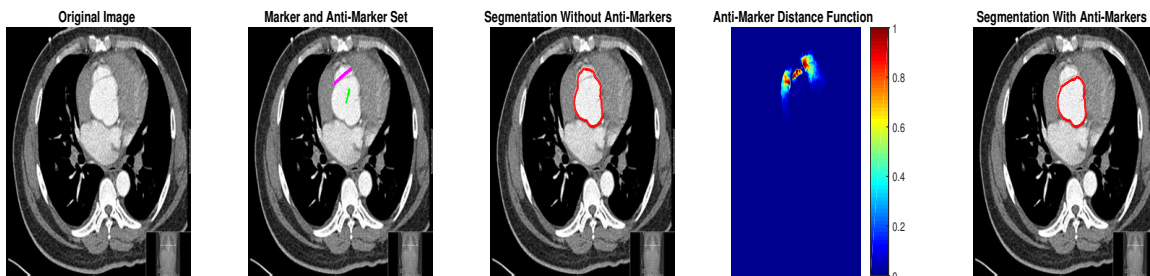


Figure 6: (Left to right:) original image, \mathcal{M} (green) and \mathcal{AM} (pink), segmentation result just using marker set, $\mathcal{D}_{AM}(x, y)$ using anti-markers, segmentation result using anti-markers. For these $\mu = 1, \lambda_1 = \lambda_2 = 5, \theta = 25$.

280 the set \mathcal{AM} denoted by $\mathcal{D}_{AM}(x, y)$ which penalises pixels near to the set \mathcal{AM} and doesn't add
 281 any penalty to those far away. We could naively choose $\mathcal{D}_{AM}(x, y) = 1 - \tilde{\mathcal{D}}_{GAM}(x, y)$ where
 282 $\tilde{\mathcal{D}}_{GAM}(x, y)$ is the normalised geodesic distance from \mathcal{AM} . However this puts a large penalty
 283 on those pixels inside the object we actually want to segment (as $\tilde{\mathcal{D}}_{GAM}(x, y)$ to those pixels is
 284 small). To avoid this problem, we propose the following anti-marker distance term
 285

$$\mathcal{D}_{AM}(x, y) = \frac{\exp(-\tilde{\alpha}\tilde{\mathcal{D}}_{GAM}(x, y)) - \exp(-\tilde{\alpha})}{1 - \exp(-\tilde{\alpha})}$$

286 where $\tilde{\alpha}$ is a tuning parameter. We choose $\tilde{\alpha} = 200$ throughout. This distance term ensures
 287 rapid decay of the penalty away from the set \mathcal{AM} but still enforces high penalty around the
 288 anti-marker set itself. See Figure 6 where a segmentation result with and without anti-markers is
 289 shown. As $\mathcal{D}_{AM}(x, y)$ decays rapidly from \mathcal{AM} , we do require that the anti-marker set be close
 290 to the blurred edge and away from the object we desire to segment.

291 3.4. The new model and its Euler-Lagrange equation

292 **The Proposed Geodesic Model.** Putting the above 3 ingredients together, we propose the model

$$\min_{u, c_1, c_2} \left\{ F_{GEO}(u, c_1, c_2) = \int_{\Omega} \left[\lambda_1(z(x, y) - c_1)^2 - \lambda_2(z(x, y) - c_2)^2 \right] u \, d\Omega \right. \\ \left. + \mu \int_{\Omega} g(|\nabla z(x, y)|) |\nabla u| \, d\Omega + \theta \int_{\Omega} \mathcal{D}_G(x, y) u \, d\Omega + \alpha \int_{\Omega} v_{\varepsilon}(u) \, d\Omega \right\}, \quad (18)$$

where $\mathcal{D}_G(x, y) = (\mathcal{D}_M(x, y) + \mathcal{D}_{AM}(x, y)) / 2$ and $\mathcal{D}_M(x, y)$ is the geodesic distance from the marker set \mathcal{M} . We compute $\mathcal{D}_M(x, y)$ using (11) where $f(x, y) = f_2(x, y)$ defined in (17). Using Calculus of Variations, solving (18) with respect to c_1, c_2 , with u fixed, leads to

$$c_1(u) = \frac{\int_{\Omega} u \cdot z(x, y) \, d\Omega}{\int_{\Omega} u \, d\Omega}, \quad c_2(u) = \frac{\int_{\Omega} (1 - u) \cdot z(x, y) \, d\Omega}{\int_{\Omega} (1 - u) \, d\Omega}, \quad (19)$$

and the minimisation with respect to u (with c_1 and c_2 fixed) gives the PDE

$$\mu \nabla \cdot \left(g(|\nabla z(x, y)|) \frac{\nabla u}{|\nabla u|_{\varepsilon_2}} \right) - \left[\lambda_1(z(x, y) - c_1)^2 - \lambda_2(z(x, y) - c_2)^2 \right] \\ - \theta \mathcal{D}_G(x, y) - \alpha v'_{\varepsilon}(u) = 0 \quad (20)$$

in Ω , where we replace $|\nabla u|$ with $|\nabla u|_{\varepsilon_2} = \sqrt{u_x^2 + u_y^2 + \varepsilon_2}$ to avoid zero denominator; we choose $\varepsilon_2 = 10^{-6}$ throughout. We also have Neumann boundary conditions $\frac{\partial u}{\partial \mathbf{n}} = 0$ on $\partial\Omega$ where \mathbf{n} is the outward unit normal vector.

Next we discuss a numerical scheme for solving this PDE (20). However it should be remarked that updating $c_1(u), c_2(u)$ should be done as soon as u is updated; practically c_1, c_2 converge very quickly since the object intensity c_1 does not change much.

4. AN ADDITIVE OPERATOR SPLITTING ALGORITHM

Additive Operator Splitting (AOS) is a widely used method [14, 27, 43] as seen from more recent works [2, 3, 4, 5, 37, 39] on the diffusion type equation such as

$$\frac{\partial u}{\partial t} = \mu \nabla \cdot (G(u) \nabla u) - f. \quad (21)$$

AOS allows us to split the two dimensional problem into two one-dimensional problems, which we solve and then combine. Each one dimensional problem gives rise to a tridiagonal system of equations which can be solved efficiently, hence AOS is a very efficient method for solving diffusion-like equations. AOS is a semi-implicit method and permits far larger time-steps than the corresponding explicit schemes would. Hence AOS is more stable than an explicit method [43]. We rewrite the above equation as

$$\frac{\partial u}{\partial t} = \mu \left(\partial_x (G(u) \partial_x u) + \partial_y (G(u) \partial_y u) \right) - f.$$

and after discretisation, we can rewrite this as [43]

$$u^{k+1} = \frac{1}{2} \sum_{\ell=1}^2 \left(I - 2\tau \mu A_{\ell}(u^k) \right)^{-1} \left(u^k + \tau f \right)$$

where τ is the time-step, $A_1(u) = \partial_x(G(u)\partial_x)$ and $A_2(u) = \partial_y(G(u)\partial_y)$. For notational convenience we write $G = G(u)$. The matrix $A_1(u)$ can be obtained as follows

$$\left(A_1(u^k) u^{k+1} \right)_{i,j} = \left(\partial_x (G \partial_x u^{k+1}) \right)_{i,j} = \left(\frac{G_{i+\frac{1}{2},j}}{h_x^2} \right) u_{i+1,j}^{k+1} + \left(\frac{G_{i-\frac{1}{2},j}}{h_x^2} \right) u_{i-1,j}^{k+1} - \left(\frac{G_{i+\frac{1}{2},j} + G_{i-\frac{1}{2},j}}{h_x^2} \right) u_{i,j}^{k+1}$$

and similarly to [37, 39], for the half points in G we take the average of the surrounding pixels, e.g. $G_{i+\frac{1}{2},j} = \frac{G_{i+1,j}+G_{i,j}}{2}$. Therefore we must solve two tridiagonal systems to obtain u^{k+1} , the Thomas algorithm allows us to solve each of these efficiently [43]. The AOS method described here assumes f does not depend on u , however in our case it depends on $v'_\varepsilon(u)$ (see (20)) which has jumps around 0 and 1, so the algorithm has stability issues. This was noted in [39] and the authors adapted the formulation of (20) to offset the changes in f . Here we repeat their arguments for adapting AOS when the exact penalty term $v'_\varepsilon(u)$ is present (we refer to Figures 7 and 8 for plots of the penalty function and its derivative, respectively).

The main consideration is to extract a linear part out of the nonlinearity in $f = f(u)$. If we evaluate the Taylor expansion of $v'_\varepsilon(u)$ around $u = 0$ and $u = 1$ and group the terms into the constant and linear components in u , we can respectively write $v'_\varepsilon(u) = a_0(\varepsilon) + b_0(\varepsilon)u + \mathcal{O}(u^2)$ and $v'_\varepsilon(u) = a_1(\varepsilon) + b_1(\varepsilon)u + \mathcal{O}(u^2)$. We actually find that $b_0(\varepsilon) = b_1(\varepsilon)$ and denote the linear term as b from now on. Therefore, for a change in u of δu around $u = 0$ and $u = 1$, we can approximate the change in $v'_\varepsilon(u)$ by $b \cdot \delta u$. To focus on the jumps, define the interval in which

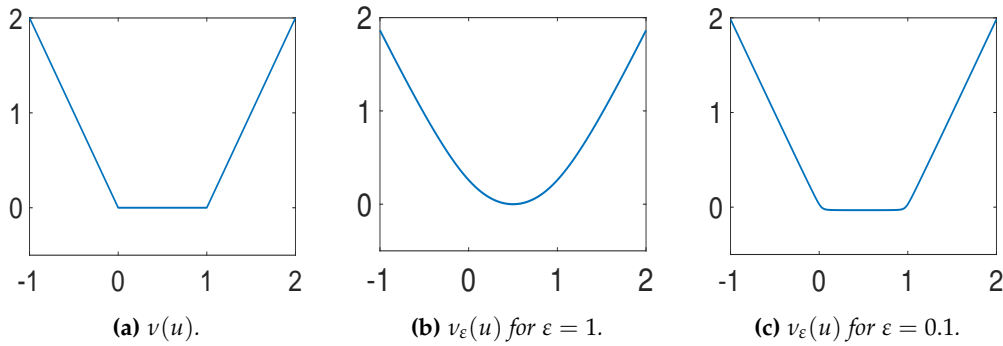


Figure 7: (a) The exact penalty function $v(u)$ and (b,c) $v_\varepsilon(u)$ for different ε values.

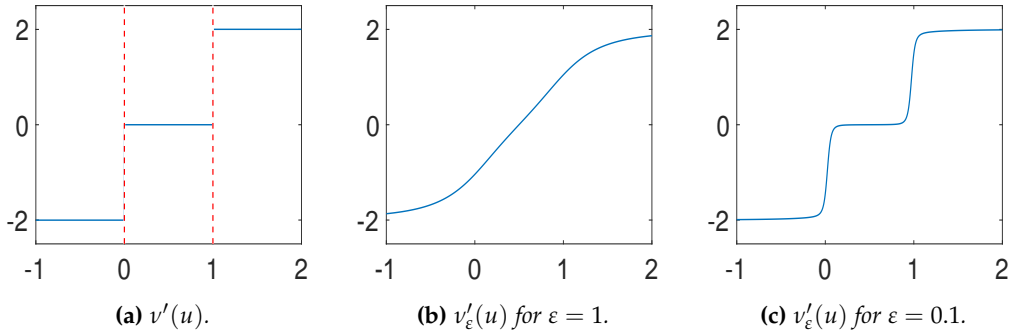


Figure 8: (a) $v'(u)$ (discontinuities shown in red) and (b,c) $v'_\varepsilon(u)$ for different ε values.

$v'_\varepsilon(u)$ jumps as

$$I_\zeta := [0 - \zeta, 0 + \zeta] \cup [1 - \zeta, 1 + \zeta]$$

and refine the linear function by

$$\tilde{b}_{i,j}^k = \begin{cases} b, & u_{i,j}^k \in I_\zeta \\ 0, & \text{else.} \end{cases}$$

Using these we can now offset the change in $v'_\varepsilon(u^k)$ by changing the formulation (21) to

$$\frac{\partial u}{\partial t} = \mu \nabla \cdot (G(u) \nabla u) - \alpha \tilde{b}^k u + [\alpha \tilde{b}^k u - f]$$

or in AOS form $u^{k+1} = u^k + \tau \mu \nabla \cdot (G(u^k) \nabla u^{k+1}) - \tau \alpha \tilde{b}^k u^{k+1} + [\tau \alpha \tilde{b}^k u^k - f^k]$ which, following the derivation in [39], can be reformulated as

$$u^{k+1} = \frac{1}{2} \sum_{\ell=1}^2 \underbrace{\left(I + \tilde{B}^k - 2\tau \mu A_\ell(u^k) \right)}_{Q_1}^{-1} \left((I + \tilde{B}^k) u^k + \tau f^k \right)$$

where $\tilde{B}^k = \text{diag}(\tau \alpha \tilde{b}^k)$. We note that Q_1 is invertible as it is strictly diagonally dominant. This scheme improves on (21) as now, changes in f^k are damped. However, it is found in [39] that although this scheme does satisfy most of the discrete scale space conditions of Weickert [43] (which guarantee convergence of the scheme), it does not satisfy all of them. In particular the matrix Q_1 doesn't have unit row sum and is not symmetrical. The authors adapt the scheme above to the equivalent

$$u^{k+1} = \frac{1}{2} \sum_{\ell=1}^2 \underbrace{\left(I - 2\tau \mu (I + \tilde{B}^k)^{-1} A_\ell(u^k) \right)}_{Q_2}^{-1} \left(u^k + \tau (I + \tilde{B}^k)^{-1} f^k \right), \quad (22)$$

where the matrix Q_2 does have unit row sum, however the matrix is not always symmetrical. We can guarantee convergence for $\zeta = 0.5$ (in which case Q_2 must be symmetrical) but we desire to use a small ζ to give a small interval I_ζ . We find experimentally that convergence is achieved for any small value of ζ , this is due to the fact that at convergence the solution u is almost binary [10]. Therefore, although initially Q_2 is asymmetrical at some pixels, at convergence all pixels have values which fall within I_ζ and $I + \tilde{B}^k$ is a matrix with all diagonal entries $1 + \tau \alpha b$. Therefore we find that at convergence Q_2 is symmetrical and the discrete scale space conditions are all satisfied. In all of our tests we fix $\zeta = 0.01$.

Algorithm 1: Solution of the Geodesic Model

Set μ, λ, θ . Compute $g(|\nabla z(x, y)|) = \frac{1}{1 + \beta_G |\nabla z(x, y)|^2}$ and $\mathcal{D}_G(x, y) = \frac{\mathcal{D}_G^0(x, y)}{\|\mathcal{D}_G^0(x, y)\|_{L^\infty}}$,

with $\mathcal{D}_G^0(x, y)$ the solution of (11). Initialise $u^{(0)}$ arbitrarily.

for $iter = 1$ to $max_iterations$ **do**

 Calculate c_1 and c_2 using (19).

 Calculate $r = \lambda_1(z - c_1)^2 - \lambda_2(z - c_2)^2 + \theta \mathcal{D}_G$.

 Set $\alpha = \|r\|_{L^\infty}$.

 Calculate $f^k = r + \alpha v'_\varepsilon(u^k)$.

 Update u^k to u^{k+1} using the AOS scheme (22).

end for

$u^* \leftarrow u^k$.

5. EXISTENCE AND UNIQUENESS OF THE VISCOSITY SOLUTION

In this section we use the viscosity solution framework and the work of Ishii and Sato [20] to prove that, for a class of PDEs in image segmentation, the solution exists and is unique. In

particular, we prove the existence and uniqueness of the viscosity solution for the PDE which is determined by the Euler-Lagrange equation for the Geodesic Model. Throughout, we will assume Ω is a bounded domain with C^1 boundary.

From the work of [12, 20], we have the following Theorem for analysing the solution of a partial differential equation of the form $F(x, u, Du, D^2u) = 0$ where $F : \mathbb{R}^n \times \mathbb{R} \times \mathbb{R}^n \times \mathcal{M}^n \rightarrow \mathbb{R}$, \mathcal{M}^n is the set of $n \times n$ symmetric matrices, Du is the gradient of u and D^2u is the Hessian of u . For simplicity, and in a slight abuse of notation, we use $x := x$ for the vector of a general point in \mathbb{R}^n .

Theorem 2 (Theorem 3.1 [20]). *Assume that the following conditions (C1)–(C2) and (I1)–(I7) hold. Then for each $u_0 \in C(\overline{\Omega})$ there is a unique viscosity solution $u \in C([0, T] \times \overline{\Omega})$ of (23) and (24) satisfying (25).*

$$\frac{\partial u}{\partial t} + F(t, x, u, Du, D^2u) = 0 \quad \text{in} \quad Q = (0, T) \times \Omega, \quad (23)$$

$$B(x, Du) = 0 \quad \text{in} \quad S = (0, T) \times \partial\Omega, \quad (24)$$

$$u(0, x) = u_0(x) \quad \text{for} \quad x \in \overline{\Omega}. \quad (25)$$

Conditions (C1)–(C2).

(C1) $F(t, x, u, p, X) \leq F(t, x, v, p, X)$ for $u \leq v$.

(C2) $F(t, x, u, p, X) \leq F(t, x, u, p, Y)$ for $X, Y \in \mathcal{M}^n$ and $Y \leq X$.

Conditions (I1)–(I7). Assume Ω is a bounded domain in \mathbb{R}^n with C^1 boundary.

(I1) $F \in C([0, T] \times \overline{\Omega} \times \mathbb{R} \times (\mathbb{R}^n \setminus \{0\}) \times \mathcal{M}^n)$.

(I2) There exists a constant $\gamma \in \mathbb{R}$ such that for each $(t, x, p, X) \in [0, T] \times \overline{\Omega} \times (\mathbb{R}^n \setminus \{0\}) \times \mathcal{M}^n$ the function $u \mapsto F(t, x, u, p, X) - \gamma u$ is non-decreasing on \mathbb{R} .

(I3) F is continuous at $(t, x, u, 0, 0)$ for any $(t, x, u) \in [0, T] \times \overline{\Omega} \times \mathbb{R}$ in the sense that

$$-\infty < F_*(t, x, u, 0, 0) = F^*(t, x, u, 0, 0) < \infty$$

holds. Here F^* and F_* denote, respectively, the upper and lower semi-continuous envelopes of F , which are defined on $[0, T] \times \overline{\Omega} \times \mathbb{R} \times \mathbb{R}^n \times \mathcal{M}^n$.

(I4) $B \in C(\mathbb{R}^n \times \mathbb{R}^n) \cap C^{1,1}(\mathbb{R}^n \times (\mathbb{R}^n \setminus \{0\}))$, where $C^{1,1}$ is the Hölder functional space.

(I5) For each $x \in \mathbb{R}^n$ the function $p \mapsto B(x, p)$ is positively homogeneous of degree one in p , i.e. $B(x, \lambda p) = \lambda B(x, p)$ for all $\lambda \geq 0$ and $p \in \mathbb{R}^n \setminus \{0\}$.

(I6) There exists a positive constant Θ such that $\langle \mathbf{n}(x), D_p B(x, p) \rangle \geq \Theta$ for all $x \in \partial\Omega$ and $p \in \mathbb{R}^n \setminus \{0\}$. Here $\mathbf{n}(x)$ denotes the unit outward normal vector of Ω at $x \in \partial\Omega$.

(I7) For each $R > 0$ there exists a non-decreasing continuous function $\omega_R : [0, \infty) \rightarrow [0, \infty)$ satisfying $\omega_R(0) = 0$ such that if $X, Y \in \mathcal{M}^n$ and $\mu_1, \mu_2 \in [0, \infty)$ satisfy

$$\begin{bmatrix} X & 0 \\ 0 & Y \end{bmatrix} \leq \mu_1 \begin{bmatrix} I & -I \\ -I & I \end{bmatrix} + \mu_2 \begin{bmatrix} I & 0 \\ 0 & I \end{bmatrix} \quad (26)$$

then

$$\begin{aligned} F(t, x, u, p, X) - F(t, y, u, q, -Y) &\geq -\omega_R\left(\mu_1\left(|x-y|^2 + \rho(p, q)^2\right) + \mu_2 + |p-q|\right) \\ &\quad + |x-y|(\max(|p|, |q|) + 1) \end{aligned}$$

for all $t \in [0, T], x, y \in \bar{\Omega}, u \in \mathbb{R}$, with $|u| \leq R, p, q \in \mathbb{R}^n \setminus \{0\}$ and $\rho(p, q) = \min\left(\frac{|p-q|}{\min(|p|, |q|)}, 1\right)$.

5.1. Existence and uniqueness for the Geodesic Model

We now prove that there exists a unique solution for the PDE (20) resulting from the minimisation of the functional for the Geodesic Model (18).

Remark 3. *It is important to note that although the values of c_1 and c_2 depend on u , they are fixed when we solve the PDE for u and therefore the problem is a local one and Theorem 2 can be applied. Once we update c_1 and c_2 , using the updated u , then we fix them again and apply Theorem 2. In practice, as we near convergence, we find c_1 and c_2 stabilise so we typically stop updating c_1 and c_2 once the change in both values is below a tolerance.*

To apply the above theorem to the proposed model (20), the key step will be to verify the nine conditions. First, we multiply (20) by the factor $|\nabla u|_{\varepsilon_2}$, obtaining the nonlinear PDE

$$-\mu |\nabla u|_{\varepsilon_2} \nabla \cdot \left(G(x, \nabla z) \frac{\nabla u}{|\nabla u|_{\varepsilon_2}} \right) + |\nabla u|_{\varepsilon_2} \left[\lambda_1 (z(x, y) - c_1)^2 - \lambda_2 (z(x, y) - c_2)^2 + \theta \mathcal{D}_G(x, y) + \alpha v'_\varepsilon(u) \right] = 0 \quad (27)$$

where $G(x, \nabla z) = g(|\nabla z(x, y)|)$. We can rewrite this as

$$F(x, u, p, X) = -\mu \text{trace}(A(x, p)X) - \mu \langle \nabla G(x, \nabla z), p \rangle + |p|k(u) + |p|f(x) = 0 \quad (28)$$

where $f(x) = \lambda_1 (z(x) - c_1)^2 - \lambda_2 (z(x) - c_2)^2$, $k(u) = \alpha v'_\varepsilon(u)$, $p = (p_1, p_2) = |\nabla u|_{\varepsilon_2}$, X is the Hessian of u and

$$A(x, p) = \begin{bmatrix} G(x, \nabla z) \frac{p_2^2}{|p|^2} & -G(x, \nabla z) \frac{p_1 p_2}{|p|^2} \\ -G(x, \nabla z) \frac{p_1 p_2}{|p|^2} & G(x, \nabla z) \frac{p_1^2}{|p|^2} \end{bmatrix} \quad (29)$$

Theorem 4 (Theory for the Geodesic Model). *The parabolic PDE $\frac{\partial u}{\partial t} + F(t, x, u, Du, D^2u) = 0$ with $u_0 = u(0, x) \in C(\bar{\Omega})$, F as defined in (28) and Neumann boundary conditions has a unique solution $u = u(t, x)$ in $C([0, T] \times \bar{\Omega})$.*

Proof. By Theorem 2, it remains to verify that F satisfies (C1)–(C2) and (I1)–(I7). We will show that each of the conditions is satisfied. Most are simple to show, the exception being (I7) which is non-trivial.

(C1): Equation (28) only has dependence on u in the term $k(u)$, we therefore have a restriction on the choice of k , requiring $k(v) \geq k(u)$ for $v \geq u$. This is satisfied for $k(u) = \alpha v'_\varepsilon(u)$ with $v'_\varepsilon(u)$ defined as in (7).

(C2): We find for arbitrary $s = (s_1, s_2) \in \mathbb{R}^2$ that $s^T A(x, p)s \geq 0$ and so $A(x, p) \geq 0$. It follows that $-\text{trace}(A(x, p)X) \leq -\text{trace}(A(x, p)Y)$, therefore this condition is satisfied.

(I1): $A(x, p)$ is only singular at $p = 0$, however it is continuous elsewhere and satisfies this condition.

(I2): In F the only term which depends on u is $k(u) = \alpha v'_\varepsilon(u)$. With $v'_\varepsilon(u)$ defined as in (7), in the limit $\varepsilon \rightarrow 0$ this function is a step function from -2 on $(\infty, 0)$, 0 on $[0, 1]$ and 2 on $(0, \infty)$. So we can choose any constant $\varepsilon < -2$. With $\varepsilon \neq 0$ there is smoothing at the end of the intervals, however there is still a lower bound on L for $v'_\varepsilon(u)$ and we can choose any constant $\gamma < L$.

1
2
3
4
5
6 413 (I3): F is continuous at $(x, 0, 0)$ for any $x \in \Omega$ because $F^*(x, 0, 0) = F_*(x, 0, 0) = 0$. Hence this
7 414 condition is satisfied.

8
9 415 (I4): The Euler-Lagrange equations give Neumann boundary conditions

$$B(x, \nabla u) = \frac{\partial u}{\partial \mathbf{n}} = \mathbf{n} \cdot \nabla u = \langle \mathbf{n}, \nabla u \rangle = 0$$

10
11
12
13
14 416 on $\partial\Omega$, where \mathbf{n} is the outward unit normal vector, and we see that $B(x, \nabla u) \in C^{1,1}(\mathbb{R}^n \times \mathbb{R}^n \setminus \{0\})$
15 417 and therefore this condition is satisfied.

16
17 418 (I5): By the definition above, $B(x, \lambda \nabla u) = \langle \mathbf{n}, \lambda \nabla u \rangle = \lambda \langle \mathbf{n}, \nabla u \rangle = \lambda B(x, \nabla u)$. So this condition
18 419 is satisfied.

19
20 420 (I6): As before we can use the definition, $\langle \mathbf{n}(x), D_p B(x, p) \rangle = \langle \mathbf{n}(x), \mathbf{n}(x) \rangle = |\mathbf{n}(x)|^2$. So we can
21 421 choose $\Theta = 1$ and the condition is satisfied.

22 422 (I7): This is the most involved condition to prove and uses many other results. For clarity of the
23 423 overall paper, we postpone the proof to Appendix A. \square

24 25 26 424 5.2. Generalisation to other related models

27
28 425 Theorems 2 and 4 can be generalised to a few other models. This amounts to writing each
29 426 model as a PDE of the form (28) where $k(u)$ is monotone and $f(x), k(u)$ are bounded. This is
30 427 summarised in the following Corollary:

31
32 428 **Corollary 5.** *Assume that c_1 and c_2 are fixed, with the terms $f(x)$ and $k(u)$ respectively defined as follows*
33 429 *for a few related models:*

- 34
35 430 • **Chan-Vese [11]**: $f(x) = f_{CV}(x) := \lambda_1(z(x) - c_1)^2 - \lambda_2(z(x) - c_2)^2, k(u) = 0$.
- 36
37 431 • **Chan-Vese (Convex) [10]**: $f(x) = f_{CV}(x), k(u) = \alpha v'_\varepsilon(u)$.
- 38
39 432 • **Geodesic Active Contours [8] and Gout et al. [25]**: $f(x) = 0, k(u) = 0$.
- 40
41 433 • **Nguyen et al. [30]**: $f(x) = \alpha (P_B(x, y) - P_F(x, y)) + (1 - \alpha) (1 - 2P(x, y)), k(u) = 0$.
- 42
43 434 • **Spencer-Chen (Convex) [39]**: $f(x) = f_{CV}(x) + \theta \mathcal{D}_E(x), k(u) = \alpha v'_\varepsilon(u)$.

44 435 Then if we define a PDE of the general form

$$-\mu \nabla \cdot \left(G(x) \frac{\nabla u}{|\nabla u|_{\varepsilon_2}} \right) + k(u) + f(x) = 0$$

45
46
47
48 436 with

49
50 437 (i) Neumann boundary conditions $\frac{\partial u}{\partial \mathbf{n}} = 0$ (\mathbf{n} the outward normal unit vector)

51
52 438 (ii) $k(u)$ satisfies $k(u) \geq k(v)$ if $u \geq v$

53
54 439 (iii) $k(u)$ and $f(x)$ are bounded; and

55
56 440 (iv) $G(x) = Id$ or $G(x) = f(|\nabla z(x)|) = \frac{1}{1 + |\nabla z(x)|^2}$,

57
58 441 we have a unique solution $u \in C([0, T] \times \overline{\Omega})$ for a given initialisation. Consequently we conclude that all
59 442 above models admit a unique solution.

443 **Proof.** The conditions (i)–(iv) are hold for all of these models. All of these models require Neu-
 444 mann boundary conditions and use the permitted $G(x)$. The monotonicity of $v'_\varepsilon(u)$ is discussed
 445 in the proof of (C1) for Theorem 4 and the boundedness of $f(x)$ and $k(u)$ is clear in all cases. \square

446 **Remark 6.** Theorem 4 and Corollary 5 also generalise to cases where $G(x) = \frac{1}{1+\beta|\nabla z|^2}$ and to $G(x) =$
 447 $\mathcal{D}(x)g(|\nabla z|)$ where $\mathcal{D}(x)$ is a distance function such as in [15, 16, 17, 39]. The proof is very similar to
 448 that shown in §5.1, relying on Lipschitz continuity of the function $G(x)$.

449 **Remark 7.** We cannot apply the classical viscosity solution framework to the Rada-Chen model [37] as
 450 this is a non-local problem with $k(u) = 2v \left(\int_{\Omega} H_\varepsilon(u) \, d\Omega - A_1 \right)$.

451 6. NUMERICAL RESULTS

452 In this section we will demonstrate the advantages of the Geodesic Model for selective image
 453 segmentation over related and previous models. Specifically we shall compare

- 454 • **M1** — the Nguyen et al. (2012) model [30];
- 455 • **M2** — the Rada-Chen (2013) model [37];
- 456 • **M3** — the convex Spencer-Chen (2015) model [39];
- 457 • **M4** — the convex Liu et al. (2017) model [26];
- 458 • **M5** — the reformulated Rada-Chen model with geodesic distance penalty (see Remark 8);
- 459 • **M6** — the reformulated Liu et al. model with geodesic distance penalty (see Remark 8);
- 460 • **M7** — the proposed convex Geodesic Model (Algorithm 1).

461 **Remark 8** (A note on **M5** and **M6**). We include **M5** – **M6** to test how the geodesic distance penalty
 462 term can improve **M2** [37] and **M4** [26]. These were obtained as follows:

- 463 • we extend **M2** to **M5** simply by including the geodesic distance function $\mathcal{D}_G(x, u)$ in the functional.
- 464 • we extend **M4** to **M6** with a minor reformulation to include data fitting terms. Specifically, the
 465 model **M6** is

$$\begin{aligned}
 \min_{u, c_1, c_2} \left\{ F_{CV\omega}(u, c_1, c_2) = \int_{\Omega} \omega^2(x, y) \left[\lambda_1(z(x, y) - c_1)^2 - \lambda_2(z(x, y) - c_2)^2 \right] u \, d\Omega \right. \\
 \left. + \mu \int_{\Omega} g(|\nabla z|) |\nabla u| \, d\Omega + \theta \int_{\Omega} \mathcal{D}_G(x, y) u \, d\Omega + \alpha \int_{\Omega} v_\varepsilon(u) \, d\Omega \right\} \quad (30)
 \end{aligned}$$

466 for $\mu, \lambda_1, \lambda_2$ non-negative fixed parameters, α and $v_\varepsilon(u)$ as defined in (7) and ω as defined for the
 467 convex Liu et al. model. This is a convex model and is the same as the proposed Geodesic Model **M7**
 468 but with weighted intensity fitting terms.

469 Four sets of test results are shown below. In Test 1 we compare models **M1** – **M6** to the proposed
 470 model **M7** for two images which are hard to segment. The first is a CT scan from which we
 471 would like to segment the lower portion of the heart, the second is an MRI scan of a knee and we
 472 would like to segment the top of the Tibia. See Figure 9 for the test images and the marker sets
 473 used in the experiments. In Test 2 we will review the sensitivity of the proposed model to the
 474 main parameters. In Test 3 we will give several results achieved by the model using marker and
 475 anti-marker sets. In Test 4 we show the initialisation independence and marker independence of
 476 the Geodesic Model on real images.

1
2
3
4
5
6 477 For **M7**, we denote by \tilde{u} the thresholded $u > \tilde{\gamma}$ at some value $\tilde{\gamma} \in (0, 1)$ to define the segmented
7 478 region. Although the threshold can be chosen arbitrarily in $(0, 1)$ from the work by [10, Thm 1]
8 479 and [39], we usually take $\tilde{\gamma} = 0.5$.

10 480 *Quantitative Comparisons.* To measure the quality of a segmentation, we use the Tanimoto Coeffi-
11 481 cient (TC) (or Jaccard Coefficient [21]) defined by

$$TC(\tilde{u}, GT) = \frac{|\tilde{u} \cap GT|}{|\tilde{u} \cup GT|}$$

16 482 where GT is the ‘ground truth’ segmentation and \tilde{u} is the result from a particular model. This
17 483 measure takes value one for a segmentation which coincides perfectly with the ground truth and
18 484 reduces to zero as the quality of the segmentation gets worse. In the other tests, where a ground
19 485 truth is not available, we use visual plots.

21 486 *Parameter Choices and Implementation.* We set $\mu = 1$, $\tau = 10^{-2}$ and vary $\lambda = \lambda_1 = \lambda_2$ and θ .
22 487 Following [10] we let $\alpha = \|\lambda_1(z - c_1)^2 - \lambda_2(z - c_2)^2 + \theta D_G(x, y)\|_{L^\infty}$. To implement the marker
23 488 points in MATLAB we use `roipoly` for choosing a small number of points by clicking and also
24 489 `freedraw` which allows the user to draw a path of marker points. The stopping criteria used
25 490 is the dynamic residual falling below a given threshold, i.e. once $\|u^{k+1} - u^k\| / \|u^k\| < tol$ the
26 491 iterations stop (we use $tol = 10^{-6}$ in the tests shown).

29 492 **Test 1 – Comparison of models M1 – M7.**

31 493 In this test we give the segmentation results for models **M1 – M7** for the two challenging test im-
32 494 ages shown in Figure 9. The marker and anti-marker sets used in the experiments are also shown
33 495 in this figure. After extensive parameter tuning, the best final segmentation results for each of
34 496 the models are shown in Figures 10 and 11. For **M1 – M4** we obtain incorrect segmentations
35 497 in both cases. In particular, the results of **M2** and **M4** are interesting as the former gives poor
36 498 results for both images, and the latter gives a reasonable result for Test Image 1 and a poor result
37 499 for Test Image 2. In the case of **M2**, the regularisation term includes the edge detector and the
38 500 distance penalty term (see (4)). It is precisely this which permits the poor result in Figures 10(b)
39 501 and 11(b) as the edge detector is zero along the contour and the fitting terms are satisfied there
40 502 (both intensity and area constraints) – the distance term is not large enough to counteract the
41 503 effect of these. In the case of **M4**, the distance term and edge detector are separated from the
42 504 regulariser and are used to weight the Chan-Vese fitting terms (see (9)). The poor segmentation
43 505 in Figure 11(b) is due to the Chan-Vese terms encouraging segmentation of bright objects (in this
44 506 case), weighting ω enforces these terms at all edges in the image and near \mathcal{M} . In experiments,
45 507 we find that **M4** performs well when the object to segment is of approximately the highest or
46 508 lowest intensity in the image, however when this is not the case, results tend to be poor. We see
47 509 that, in both cases, models **M5** and **M6** give much improved results to **M2** and **M4** (obtained by
48 510 incorporating the geodesic distance penalty into each). The proposed Geodesic Model **M7** gives
49 511 an accurate segmentation in both cases. It remains to compare **M5**, **M6** and **M7**. We see that
50 512 **M5** is a non-convex model (and cannot be made convex [39]), therefore results are initialisation
51 513 dependent. It also requires one more parameter than **M6** and **M7**, and an accurate set \mathcal{M} to give
52 514 a reasonable area constraint in (4). These limitations lead us to conclude **M6** and **M7** are better
53 515 choices than **M5**. In the case of **M6**, it has the same number of parameters as **M7** and gives good
54 516 results. **M6** can be viewed as the model **M7** with weighted intensity fitting terms (compare (18)
55 517 and (30)). Experimentally, we find that the same quality of segmentation result can be achieved
56 518 with both models generally, however **M6** is more parameter sensitive than **M7**. This can be seen

ε_2	Knee Segmentation (Figure 12)	Circle Segmentation (Figure 13)
10^{-10}	0.97287	1.00000
10^{-8}	0.97287	1.00000
10^{-6}	0.97235	1.00000
10^{-4}	0.96562	1.00000
10^{-2}	0.94463	1.00000
10^0	0.90660	1.00000
10^2	0.89573	1.00000
10^4	0.89159	1.00000

Table 1: The Tanimoto Coefficient for various ε_2 values, segmenting the images in Figures 12 and 13.

in the parameter map in Figure 12 with **M7** giving an accurate result for a wider range of parameters than **M6**. To show the improvement of **M7** over previous models, we also give an image in Figure 13 which can be accurately segmented with **M7** but the correct result is never achieved with **M6** (or **M3**). Therefore we find that **M7** outperforms all other models tested **M1** – **M6**.

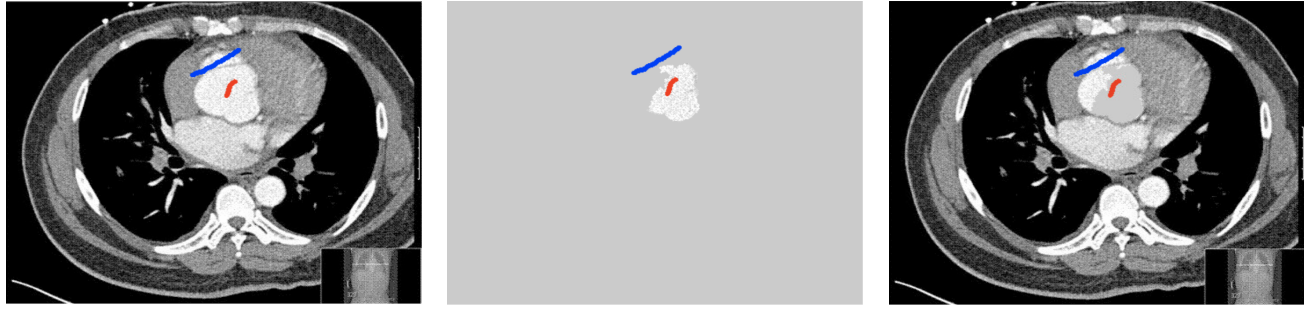
Remark 9. Models **M2** – **M7** are coded in MATLAB and use exactly the same marker/anti-marker set. For model **M1**, the software of Nguyen et al. requires marker and anti-marker sets to be input to an interface. These have been drawn as close as possible to match those used in the MATLAB code.



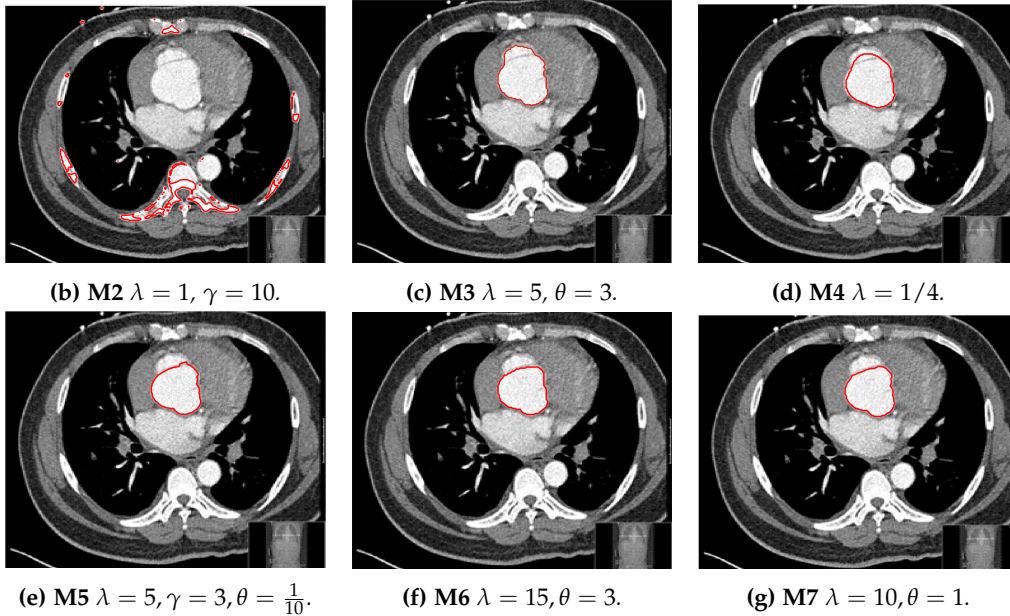
Figure 9: Test 1 setting: (i) Image 1; (ii) Image 1 with marker and anti-marker set shown in green and pink respectively; (iii) Test Image 2; (iv) Image 2 with marker set shown.

Test 2 – Test of M7’s sensitivity to changes in its main parameters. In this test we demonstrate that the proposed Geodesic Model is robust to changes in the main parameters. The main parameters in (20) are $\mu, \lambda_1, \lambda_2, \theta$ and ε_2 . In all tests we set $\mu = 1$, which is simply a rescaling of the other parameters, and we set $\lambda = \lambda_1 = \lambda_2$. In the first example, in Figure 12, we compare the TC value for various λ and θ values for segmentation of a bone in a knee scan. We see that the segmentation is very good for a larger range of θ and λ values. For the second example, in Figure 13, we show an image and marker set for which the Spencer-Chen model (**M3**) and modified Liu et al. model **M6** cannot achieve the desired segmentation for any parameter range, but which can be attained for the Geodesic Model for a vast range of parameters. The final example, in Table 1, compares the TC values for various ε_2 values with fixed parameters $\lambda = 2$ and $\theta = 2$. We use the images and ground truth as shown in Figures 12 and 13: on the synthetic circles image we obtain a perfect segmentation for all values of ε_2 tested, and in the case of the knee segmentation the results are almost identical for any $\varepsilon_2 < 10^{-6}$, above which the quality slowly deteriorates.

Test 3 – Further Results from the Geodesic Model M7. In this test we give some medical segmentation results obtained using the Geodesic Model **M7**. The results are shown in Figure 14.



(a) **M1** (Left to right:) Test Image 1 with markers (red) and anti-markers (blue), foreground segmentation and background segmentation (we used published software, no parameter choice required).



(b) **M2** $\lambda = 1, \gamma = 10$.

(c) **M3** $\lambda = 5, \theta = 3$.

(d) **M4** $\lambda = 1/4$.

(e) **M5** $\lambda = 5, \gamma = 3, \theta = \frac{1}{10}$.

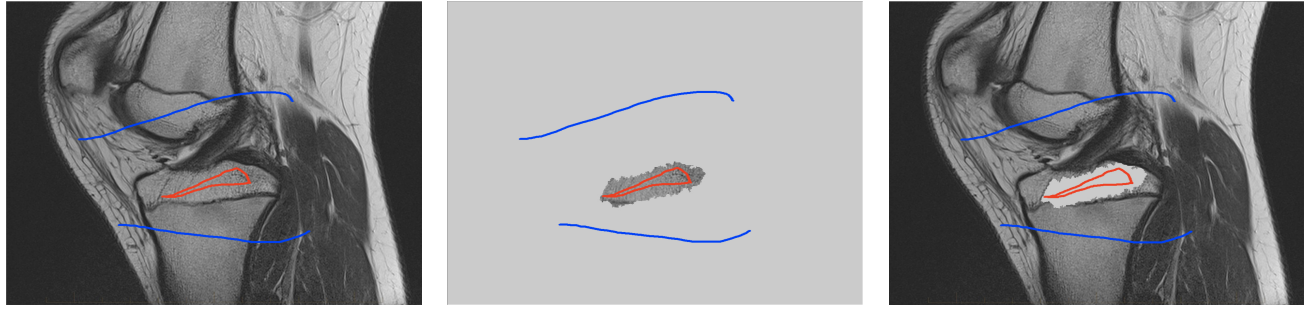
(f) **M6** $\lambda = 15, \theta = 3$.

(g) **M7** $\lambda = 10, \theta = 1$.

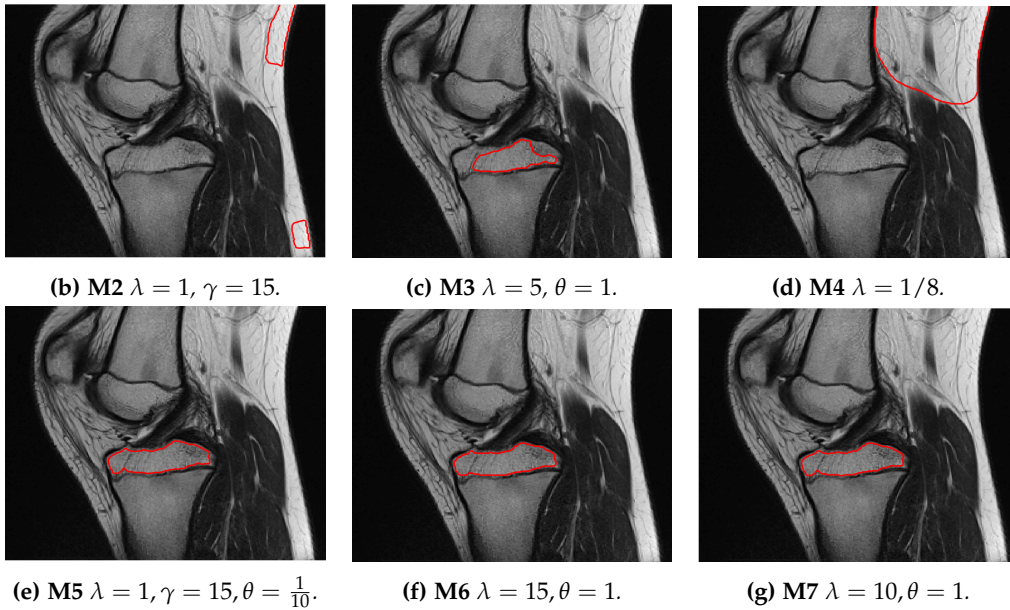
Figure 10: Visual comparison of **M1** – **M7** results for Test Image 1. **M1** segmented part of the object, **M2** – **M4** failed to segment the object, **M5** gave a reasonable result (though not accurate) and, **M6** and **M7** correctly segmented the object.

541 In the final two columns we use anti-markers to demonstrate how to overcome blurred edges
 542 and low contrast edges in an image. These are challenging and it is pleasing to see the correctly
 543 segmented results.

544 **Test 4 – Initialisation and Marker Set Independence.** In the first example, in Figure 15, we see
 545 how the convex Geodesic Model **M7** gives the same segmentation result regardless of initialisa-
 546 tion, as expected of a convex model. Hence the model is flexible in implementation. From many
 547 experiments it is found that using the polygon formed by the marker points as the initialisation
 548 converges to the final solution faster than using an arbitrary initialisation. In the second exam-
 549 ple, in Figure 16, we show intuitively how Model **M7** is robust to the number of markers and the
 550 location of the markers within the object to be segmented. The Euclidean distance term, used in
 551 the Spencer-Chen model **M3**, is sensitive to the position and number of marker points, however,



(a) **M1** (Left to right:) Test Image 2 with markers (red) and anti-markers (blue), foreground segmentation and background segmentation (we used published software, no parameter choice required).



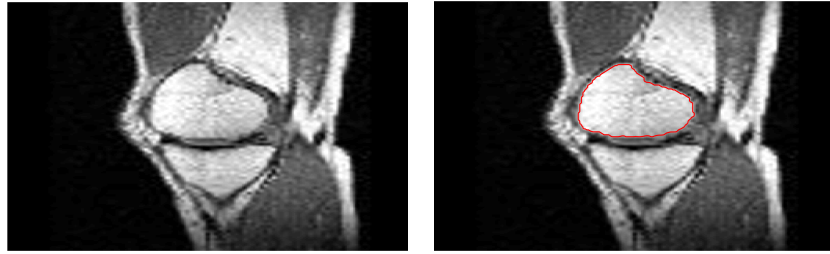
(b) **M2** $\lambda = 1, \gamma = 15$. (c) **M3** $\lambda = 5, \theta = 1$. (d) **M4** $\lambda = 1/8$.
(e) **M5** $\lambda = 1, \gamma = 15, \theta = \frac{1}{10}$. (f) **M6** $\lambda = 15, \theta = 1$. (g) **M7** $\lambda = 10, \theta = 1$.

Figure 11: Visual comparison of **M1** – **M7** results for Test Image 2. **M1** segmented part of the object, **M2** – **M4** failed to segment the object, **M5**, **M6** and **M7** correctly segmented the object.

552 regardless of where the markers are chosen, and how many are chosen, the geodesic distance
553 map will be almost identical.

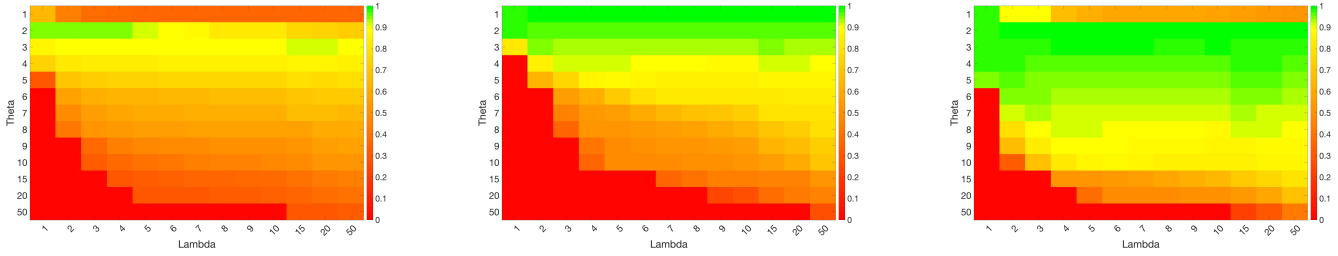
554 7. CONCLUSIONS

555 In this paper a new convex selective segmentation model has been proposed, using geodesic
556 distance as a penalty term. This model gives results that are unachievable by alternative selective
557 segmentation models and is also more robust to the parameter choices. Adaptations to the
558 penalty term have been discussed which make it robust to noisy images and blurry edges whilst
559 also penalising objects far from the marker set (in a Euclidean distance sense). A proof for
560 the existence and uniqueness of the viscosity solution to the PDE given by the Euler-Lagrange
561 equation for the model has been given (which applies to an entire class of image segmentation
562 PDEs). Finally we have confirmed the advantages of using the geodesic distance with some



(a) Original Image.

(b) Ground Truth Segmentation.

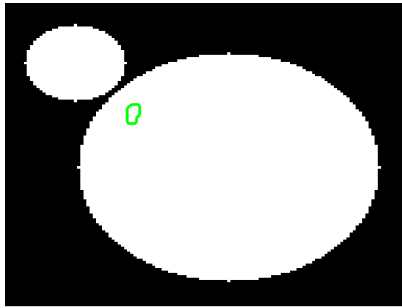


(c) M3 TC values for various λ and θ values.

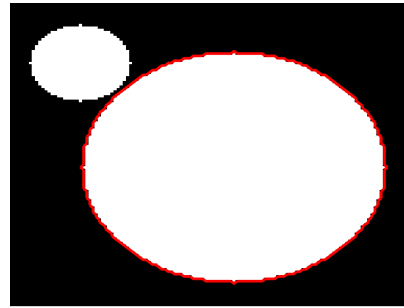
(d) M6 TC values for various λ and θ values.

(e) M7 TC values for various λ and θ values.

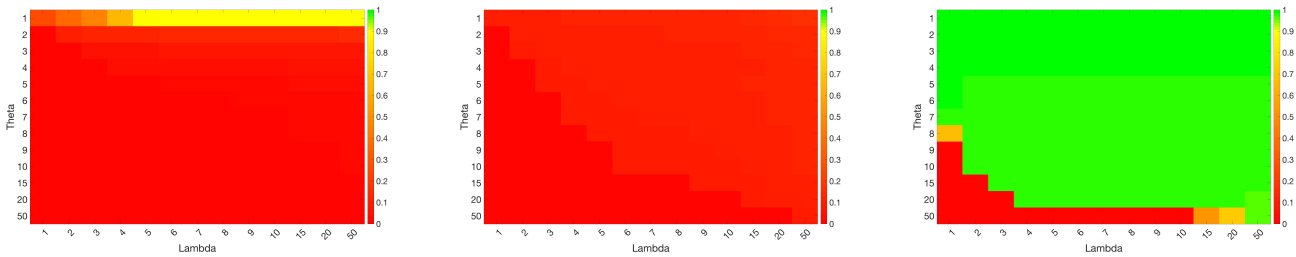
Figure 12: Parameter maps for M3, M6 and M7



(a) Original image with marker set.



(b) Ground truth segmentation.



(c) M3 TC values for various λ and θ values.

(d) M6 TC values for various λ and θ values.

(e) M7 TC values for various λ and θ values.

Figure 13: Parameter maps for M3, M6 and M7

563 experimental results. Future works will look for further extension of selective segmentation to
 564 other frameworks such as using high order regularizers [46, 13] where only incomplete theories
 565 exist.

1
2
3
4
5
6
7
8
9
10
11
12
13
14
15
16
17
18
19
20
21
22
23
24
25
26
27
28
29
30
31
32
33
34
35
36
37
38
39
40
41
42
43
44
45
46
47
48
49
50
51
52
53
54
55
56
57
58
59
60
61
62
63
64
65

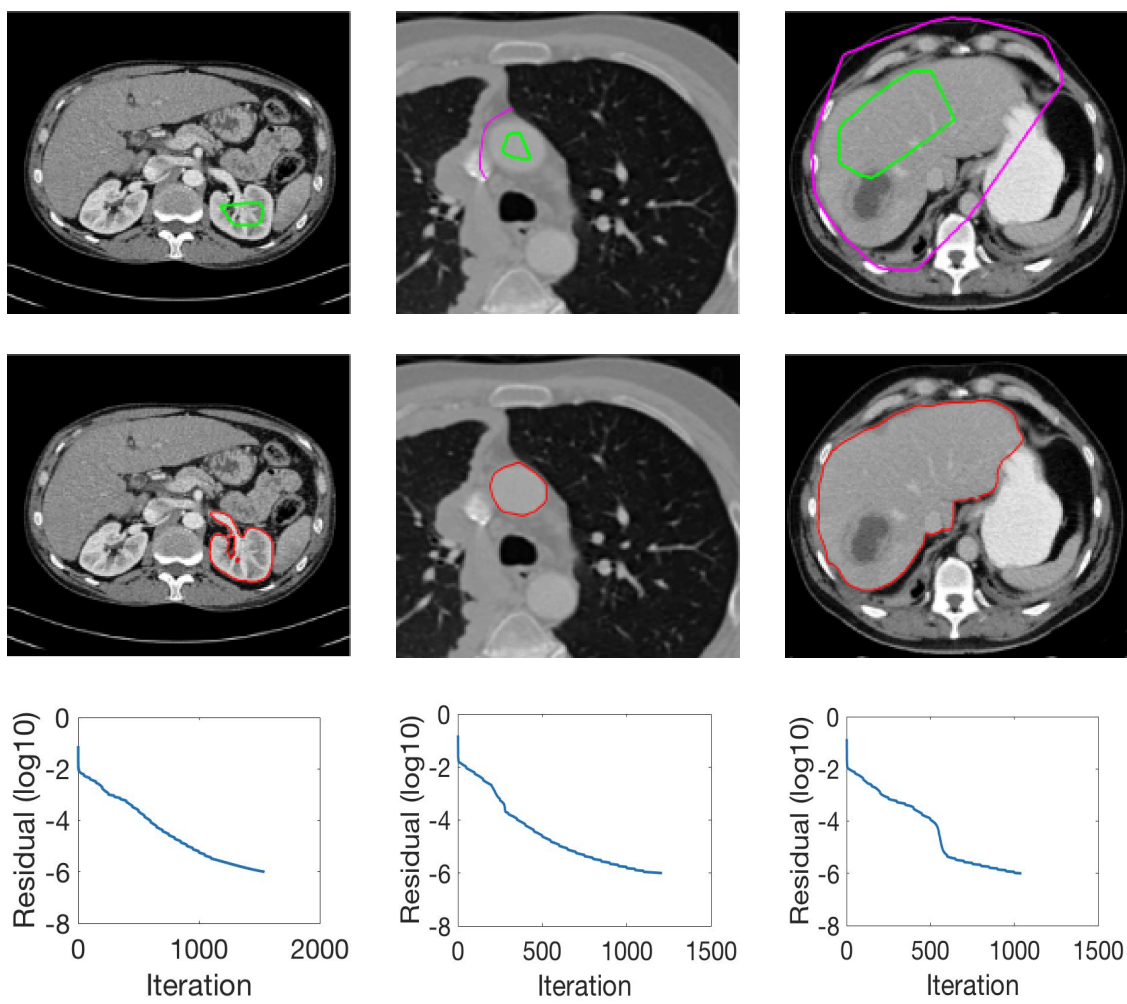


Figure 14: Three further test results obtained using our Geodesic Model **M7**, all with parameters $\theta = 5$, $\lambda = 5$. The first row shows the original image with the marker set (plus anti-marker set), the second row the final segmentation result and the final row shows the residual history.

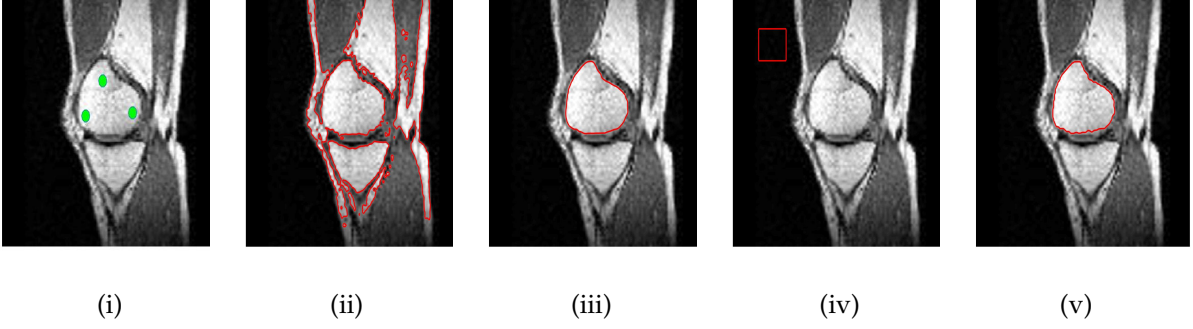


Figure 15: Test 4 on **M7**'s initialisations ($\theta = 5, \lambda = 5$). (i) The original image with marker set indicated; (ii) Initialisation 1 using the image itself; (iii) Segmentation result from Initialisation 1; (iv) Initialisation 2 away from the object to be segmented; (v) Segmentation 2 from initialisation 2. Clearly **M7** gives the same result.

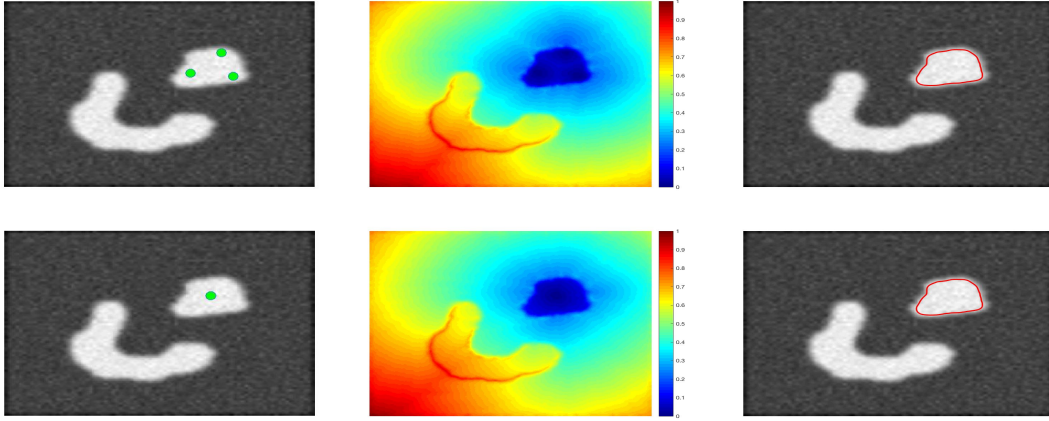


Figure 16: Test 4 on **M7**'s marker set ($\theta = 5, \lambda = 3$). Row 1 shows the original image with 3 marker points, the normalised geodesic distance map and the final segmentation result. Row 2 shows the original image with 1 marker point, the normalised geodesic distance map and the final segmentation result. Clearly the second and third columns are the same for different marker points. Thus **M7** is robust.

566 ACKNOWLEDGEMENTS

567 The authors are grateful to Professor Joachim Weickert (Saarland, Germany) for fruitful discus-
568 sions at the early stages of this work during a Newton programme in Cambridge.

569 Appendix A — PROOF THAT CONDITION (I7) HOLDS IN THEOREM 4

570 Using the assumption in (26), we write

$$\begin{aligned}
 (Xr, r) + (Ys, s) &= r^T Xr + s^T Ys \leq \mu_1 [r^T \quad s^T] \begin{bmatrix} I & -I \\ -I & I \end{bmatrix} \begin{bmatrix} r \\ s \end{bmatrix} + \mu_2 [r^T \quad s^T] \begin{bmatrix} I & 0 \\ 0 & I \end{bmatrix} \begin{bmatrix} r \\ s \end{bmatrix} \\
 &= \mu_1 |r - s|^2 + \mu_2 (|r|^2 + |s|^2).
 \end{aligned}$$

1
2
3
4
5
6
7
8
9
10
11
12
13
14
15
16
17
18
19
20
21
22
23
24
25
26
27
28
29
30
31
32
33
34
35
36
37
38
39
40
41
42
43
44
45
46
47
48
49
50
51
52
53
54
55
56
57
58
59
60
61
62
63
64
65

571 Note that matrix A from (29) is a real symmetric matrix and decomposes as $A = QDQ^T =$
572 $QD^{1/2}D^{1/2}Q^T = BB^T$ with Q orthonormal and $B = QD^{1/2}$. Successively define $r = B(p)e_i$ and
573 $s = B(p)e_i$ for all (e_i) , an orthonormal basis, and obtain

$$(Xr, r) = r^T Xr = \sum_i (Be_i)^T X(Be_i) = \sum_i e_i^T B^T XBe_i = \text{trace}(B^T X B) = \text{trace}(A(x, p)X).$$

574 Therefore, we can write

$$\begin{aligned} \text{trace}(A(x, p)X) + \text{trace}(A(y, q)Y) &= (XB(p)e_i, B(p)e_i) + (YB(q)e_i, B(q)e_i) \\ &\leq \mu_1 |B(p)e_i - B(q)e_i|^2 + \mu_2 (|B(p)e_i|^2 + |B(q)e_i|^2) \\ &= \mu_1 \text{trace} \left((B(p) - B(q))^T (B(p) - B(q)) \right) + \mu_2 (G(x) + G(y)). \end{aligned}$$

575 We now focus on reformulating the first term, we start by decomposing $A(x, p)$ as follows

$$A(x, p) = \begin{bmatrix} \frac{p_1}{|p|} & -\frac{p_2}{|p|} \\ \frac{p_2}{|p|} & \frac{p_1}{|p|} \end{bmatrix} \begin{bmatrix} 0 & 0 \\ 0 & G(x) \end{bmatrix} \begin{bmatrix} \frac{p_1}{|p|} & \frac{p_2}{|p|} \\ -\frac{p_2}{|p|} & \frac{p_1}{|p|} \end{bmatrix} = \begin{bmatrix} \frac{p_1}{|p|} & -\frac{p_2}{|p|} \\ \frac{p_2}{|p|} & \frac{p_1}{|p|} \end{bmatrix} \begin{bmatrix} 0 & 0 \\ 0 & \sqrt{G(x)} \end{bmatrix} \begin{bmatrix} 0 & 0 \\ 0 & \sqrt{G(x)} \end{bmatrix} \begin{bmatrix} \frac{p_1}{|p|} & \frac{p_2}{|p|} \\ -\frac{p_2}{|p|} & \frac{p_1}{|p|} \end{bmatrix}$$

576 so we have $A = BB^T$ where

$$B(p) = \begin{bmatrix} 0 & -\frac{p_2}{|p|} \sqrt{G(x)} \\ 0 & \frac{p_1}{|p|} \sqrt{G(x)} \end{bmatrix}.$$

577 Using this we compute

$$\text{trace} \left((B(p) - B(q))^T (B(p) - B(q)) \right) = \left| \frac{p}{|p|} \sqrt{G(x)} - \frac{q}{|q|} \sqrt{G(y)} \right|^2.$$

578 Substituting this in the overall trace sum we have

$$\text{trace}(A(x, p)X) + \text{trace}(A(y, q)Y) \leq \mu_1 \left| \frac{p}{|p|} \sqrt{G(x)} - \frac{q}{|q|} \sqrt{G(y)} \right|^2 + 2\mu_2 \theta.$$

579 as $G(x) < \theta$ (G is bounded) for all $x \in \Omega$. Focussing on the first term in this expression we
580 compute

$$\begin{aligned} \left| \frac{p}{|p|} \sqrt{G(x)} - \frac{q}{|q|} \sqrt{G(y)} \right|^2 &= \left| \frac{p}{|p|} \sqrt{G(x)} - \frac{p}{|p|} \sqrt{G(y)} + \frac{p}{|p|} \sqrt{G(y)} - \frac{q}{|q|} \sqrt{G(y)} \right|^2 \\ &\leq 2 \left(\sqrt{G(x)} - \sqrt{G(y)} \right)^2 + 2G(y) \left| \frac{p}{|p|} - \frac{q}{|q|} \right|^2 \\ &\leq 2 \left(\sqrt{G(x)} - \sqrt{G(y)} \right)^2 + 8\theta \rho(p, q)^2 \end{aligned}$$

581 where $\rho = \min \left(\frac{|p-q|}{\min(|p|, |q|)}, 1 \right)$. This uses inequality $\left| \frac{p}{|p|} - \frac{q}{|q|} \right|^2 \leq 2\rho(p, q)$ (see [15, 16, 17, 18, 24,
582 35]). We now note that $g(s) = \frac{1}{1+s^2}$ is Lipschitz continuous with Lipschitz constant $\frac{3\sqrt{3}}{8}$.

583 **Note.** In the Geodesic Model we fix $G(x) = g(|\nabla z|)$. Therefore, assuming $G(x)$ and $\sqrt{G(x)}$ as
584 Lipschitz requires us to assume that the underlying z is a smooth function [16]. Thankfully, z is
585 typically provided as a smoothed image after some filtering (e.g. Gaussian smoothing) and we
586 can assume regularity of z .

587 **Remark 10.** It is less clear that $\sqrt{G(x)}$ is Lipschitz, we now prove it explicitly. Firstly, it is relatively
 588 easy to prove that

$$\sqrt{G(x)} - \sqrt{G(y)} \leq \frac{2}{3\sqrt{3}} \left| |\nabla z(x)| - |\nabla z(y)| \right|$$

589 by letting $K(s) = \sqrt{g(s)}$ and we find $\sup_s |K'(s)| = \frac{2}{3\sqrt{3}}$. We now need to prove that $|\nabla z(x)|$ is Lipschitz
 590 also. Take $h(x) = |\nabla z(x)|$, then by a remark in [16], we can conclude $\exists \zeta < \infty$ such that

$$\left| |\nabla z(x)| - |\nabla z(y)| \right| \leq \zeta |x - y|$$

591 and so $\sqrt{G(x)}$ is Lipschitz with constant $\frac{2}{3\sqrt{3}}\zeta$.

592 After some computations we obtain

$$\left| \frac{p}{|p|} \sqrt{G(x)} - \frac{q}{|q|} \sqrt{G(y)} \right|^2 \leq 2 \left(\frac{2}{3\sqrt{3}}\zeta \right)^2 |x - y|^2 + 8\theta\rho(p, q)^2 = \frac{8}{27}\zeta^2 |x - y|^2 + 8\theta\rho(p, q)^2.$$

593 Following the results in [15, 16, 17, 18, 24, 35] we have

$$|\nabla G(x) - \nabla G(y)| |p| < \kappa |p| |x - y| \leq \kappa \max(|p|, |q|) |x - y|.$$

594 so overall

$$\langle \nabla G(x), p \rangle - \langle \nabla G(y), q \rangle \leq \kappa \max(|p|, |q|) |x - y| + \eta |p - q|$$

595 where $|\nabla G(y)| < \eta < \infty$. Finally, we note that $-(|p| - |q|) = |q| - |p| \leq \left| |q| - |p| \right| \leq |p - q|$. If
 596 we now write

$$\begin{aligned} & - (F(t, x, u, p, X) - F(t, y, u, q, -Y)) = \mu (\text{trace}(A(x, p)X) + \text{trace}(A(y, q)Y)) \\ & \quad + \mu (\langle \nabla G(x), p \rangle - \langle \nabla G(y), q \rangle) \\ & \quad - (|p| - |q|)k(u) - |p|f(x) + |q|f(y) \\ & \leq \mu\mu_1 \left(\frac{8}{27}\zeta^2 |x - y|^2 + 8\theta\rho(p, q)^2 \right) + 2\mu\mu_2\theta \\ & \quad + \mu\kappa \max(|p|, |q|) |x - y| + \mu\eta |p - q| \\ & \quad - (|p| - |q|) \left(k(u) + 2 \max_{x \in \Omega} f(x) \right) \\ & \leq \mu\mu_1 \left(\frac{8}{27}\zeta^2 |x - y|^2 + 8\theta\rho(p, q)^2 \right) + 2\mu\mu_2\theta \\ & \quad + \mu\kappa (\max(|p|, |q|) + 1) |x - y| + \mu\eta |p - q| + C_1 |p - q|. \end{aligned}$$

597 where $C_1 = \max_{x \in \Omega} \left(k(u) + 2 \max_{x \in \Omega} f(x) \right)$ (we must assume $k(u), f(x)$ are bounded). Hence we have

$$\begin{aligned} & F(t, x, u, p, X) - F(t, y, u, q, -Y) \geq \\ & \quad - \max \left\{ \frac{8}{27}\zeta^2\mu, 8\mu\theta, 2\mu\theta, \mu\eta + C_1, \mu\kappa \right\} \left[\mu_1 \left(|x - y|^2 + \rho(p, q)^2 \right) + \mu_2 \right. \\ & \quad \left. + |p - q| + |x - y| (\max(|p|, |q|) + 1) \right] \end{aligned}$$

598 and setting $\omega_R = \max \left\{ \frac{8}{27}\zeta^2\mu, 8\mu\theta, 2\mu\theta, \mu\eta + C_1, \mu\kappa \right\} R$, this is a non-decreasing continuous func-
 599 tion, maps $[0, \infty) \rightarrow [0, \infty)$ and $\omega_R(0) = 0$ as required. We have proven that condition (I7) is
 600 satisfied.

1
2
3
4
5
6 001 REFERENCES

- 7
8 002 [1] R. Adams and L. Bischof. Seeded region growing. *IEEE Transactions on Pattern Analysis and*
9 003 *Machine Intelligence*, 16(6):641–647, 1994.
- 10
11 004 [2] N. Badshah and Ke Chen. Multigrid Method for the Chan-Vese Model in Variational Seg-
12 005 *mentation*. *Communications in Computational Physics*, 4(2):294–316, 2008.
- 13
14 006 [3] N. Badshah and Ke Chen. On two multigrid algorithms for modeling variational multiphase
15 007 *image segmentation*. *IEEE Transactions on Image Processing*, 18(5):1097–1106, 2009.
- 16
17 008 [4] N. Badshah and Ke Chen. Image selective segmentation under geometrical constraints using
18 009 *an active contour approach*. *Communications in Computational Physics*, 7(4):759–778, 2010.
- 19
20 010 [5] N. Badshah, Ke Chen, H. Ali, and G. Murtaza. A coefficient of variation based image
21 011 *selective segmentation model using active contours*. *East Asian J. Appl. Math.*, 2:150–169,
22 012 2012.
- 23
24 013 [6] Xue Bai and Guillermo Sapiro. Geodesic matting: A framework for fast interactive image
25 014 *and video segmentation and matting*. *International journal of computer vision*, 82(2):113–132,
26 015 2009.
- 27
28 016 [7] Dhruv Batra, Adarsh Kowdle, Devi Parikh, Jiebo Luo, and Tsuhan Chen. *Interactive co-*
29 017 *segmentation of objects in image collections*. Springer Science & Business Media, 2011.
- 30
31 018 [8] Vicent Caselles, Ron Kimmel, and Guillermo Sapiro. Geodesic Active Contours. *International*
32 019 *Journal of Computer Vision*, 22(1):61–79, 1997.
- 33
34 020 [9] Francine Catté, Pierre-Louis Lions, Jean-Michel Morel, and Tomeu Coll. Image selective
35 021 *smoothing and edge detection by nonlinear diffusion*. *SIAM Journal on Numerical analysis*,
36 022 29(1):182–193, 1992.
- 37
38 023 [10] Tony F. Chan, Selim Esedoglu, and Mila Nikolova. Algorithms for Finding Global Mini-
39 024 *mizers of Image Segmentation and Denoising Models*. *SIAM Journal on Applied Mathematics*,
40 025 66(5):1632–1648, 2006.
- 41
42 026 [11] Tony F. Chan and Luminita A. Vese. Active contours without edges. *IEEE Transactions on*
43 027 *Image Processing*, 10(2):266–277, 2001.
- 44
45 028 [12] M. G. Crandall, H. Ishii, and P.-L. Lions. User’s guide to viscosity solutions of second order
46 029 *partial differential equations*. *ArXiv Mathematics e-prints*, June 1992.
- 47
48 030 [13] J. Duan, W. Lu, Z. Pan, and L. Bai. New second order mumford-shah model based on Γ -
49 031 *convergence approximation for image processing*. *Infrared Physics and Technology*, 76:641–647,
50 032 2016.
- 51
52 033 [14] D. G. Gordeziani and G.V. Meladze. Simulation of the third boundary value problem for
53 034 *multidimensional parabolic equations in an arbitrary domain by one-dimensional equations*.
54 035 *USSR Computational Mathematics and Mathematical Physics*, 14:249–253, 1974.
- 55
56 036 [15] Christian Gout and Carole Le Guyader. Segmentation of complex geophysical structures
57 037 *with well data*. *Computational Geosciences*, 10(4):361–372, 2006.
- 58
59 038 [16] Christian Gout, Carole Le Guyader, and Luminita Vese. Image segmentation under interpo-
60 039 *lation conditions*. *Preprint CAM-IPAM*, page 44 pages, 2003.

-
- 1
2
3
4
5
6 640 [17] Christian Gout, Carole Le Guyader, and Luminita A. Vese. Segmentation under geomet-
7 641 rical conditions using geodesic active contours and interpolation using level set methods.
8 642 *Numerical Algorithms*, 39(1-3):155–173, 2005.
- 9
10 643 [18] Laurence Guillot and Maïtine Bergounioux. Existence and uniqueness results for the gra-
11 644 dient vector flow and geodesic active contours mixed model. *arXiv preprint math/0702255*,
12 645 2007.
- 13
14 646 [19] Jia He, Chang-Su Kim, and C-C Jay Kuo. *Interactive Segmentation Techniques: Algorithms and*
15 647 *Performance Evaluation*. Springer Science & Business Media, 2013.
- 16
17 648 [20] Hitoshi Ishii and Moto-Hiko Sato. Nonlinear oblique derivative problems for singular de-
18 649 generate parabolic equations on a general domain. *Nonlinear Analysis: Theory, Methods and*
19 650 *Applications*, 57(7):1077 – 1098, 2004.
- 20
21 651 [21] Paul Jaccard. The distribution of the flora in the alpine zone.1. *New Phytologist*, 11(2):37–50,
22 652 1912.
- 23
24 653 [22] Michael Kass, Andrew Witkin, and Demetri Terzopoulos. Snakes: Active contour models.
25 654 *International Journal of Computer Vision*, 1(4):321–331, 1988.
- 26
27 655 [23] M. Klodt, F. Steinbrücker, and Daniel Cremers. Moment Constraints in Convex Optimization
28 656 for Segmentation and Tracking. *Advanced Topics in Computer Vision*, pages 1–29, 2013.
- 29
30 657 [24] Carole Le Guyader. *Imagerie Mathématique: segmentation sous contraintes géométriques Théorie*
31 658 *et Applications*. PhD thesis, INSA de Rouen, 2004.
- 32
33 659 [25] Carole Le Guyader and Christian Gout. Geodesic active contour under geometrical condi-
34 660 tions: Theory and 3D applications. *Numerical Algorithms*, 48(1-3):105–133, 2008.
- 35
36 661 [26] Chunxiao Liu, Michael Kwok-Po Ng, and Tiejong Zeng. Weighted variational model for se-
37 662 lective image segmentation with application to medical images. *Pattern Recognition*, pages –,
38 663 2017.
- 39
40 664 [27] T. Lu, P. Neittaanmäki, and X-C. Tai. A parallel splitting up method and its application to
41 665 navier-stokes equations. *Applied Mathematics Letters*, 4(2):25 – 29, 1991.
- 42
43 666 [28] Calvin R Maurer, Rensheng Qi, and Vijay Raghavan. A linear time algorithm for comput-
44 667 ing exact euclidean distance transforms of binary images in arbitrary dimensions. *IEEE*
45 668 *Transactions on Pattern Analysis and Machine Intelligence*, 25(2):265–270, 2003.
- 46
47 669 [29] D. Mumford and J. Shah. Optimal approximation of piecewise smooth functions ans associ-
48 670 ated variational problems. *Commu. Pure and Applied Mathematics*, 42:577–685, 1989.
- 49
50 671 [30] Thi Nhat Anh Nguyen, Jianfei Cai, Juyong Zhang, and Jianmin Zheng. Robust interactive
51 672 image segmentation using convex active contours. *IEEE transactions on image processing : a*
52 673 *publication of the IEEE Signal Processing Society*, 21(8):3734–43, 2012.
- 53
54 674 [31] S. Osher and J. Sethian. Fronts propagating with curvature-dependent speed: algorithms
55 675 based on Hamilton-Jacobi formulations. *Journal of Computational Physics*, 79(1):12–49, 1988.
- 56
57 676 [32] S. M. Patel and J. N. Dharwa. Accurate detection of abnormal tissues of brain MR images
58 677 using hybrid clustering and deep learning based classifier methods of image segmentation.
59 678 *International Journal of Innovative Research in Science, Engineering and Technology*, 6, 2017.

-
- 1
2
3
4
5
6 679 [33] Pietro Perona and Jitendra Malik. Scale-space and edge detection using anisotropic diffusion.
7 680 *IEEE Transactions on pattern analysis and machine intelligence*, 12(7):629–639, 1990.
- 8
9 681 [34] Alexis Protiere and Guillermo Sapiro. Interactive image segmentation via adaptive weighted
10 682 distances. *IEEE Transactions on image Processing*, 16(4):1046–1057, 2007.
- 11 683 [35] Lavdie Rada. *Variational models and numerical algorithms for selective image segmentation*. PhD
12 684 thesis, University of Liverpool, 2013.
- 13
14 685 [36] Lavdie Rada and Ke Chen. A new variational model with dual level set functions for selective
15 686 segmentation. *Communications in Computational Physics*, 12(1):261–283, 2012.
- 16
17 687 [37] Lavdie Rada and Ke Chen. Improved Selective Segmentation Model Using One Level-Set.
18 688 *Journal of Algorithms and Computational Technology*, 7(4):509–540, 2013.
- 19
20 689 [38] James A Sethian. A fast marching level set method for monotonically advancing fronts.
21 690 *Proceedings of the National Academy of Sciences*, 93(4):1591–1595, 1996.
- 22
23 691 [39] Jack Spencer and Ke Chen. A Convex and Selective Variational Model for Image Segmenta-
24 692 tion. *Communications in Mathematical Sciences*, 13(6):1453–1472, 2015.
- 25
26 693 [40] L. Vincent and P. Soille. Watersheds in digital spaces: an efficient algorithm based on im-
27 694 mersion simulations. *IEEE Trans. Pattern Analysis Machine Intell.*, 13(6):583–598, 1991.
- 28
29 695 [41] G. T. Wang, W. Q. Li, S. Ourselin, and T. Vercauteren. Automatic brain tu-
30 696 mor segmentation using cascaded anisotropic convolutional neural networks.
31 697 <https://arxiv.org/pdf/1709.00382.pdf>, preprint, 2017.
- 32
33 698 [42] G. T. Wang, W. Q. Li, M. A. Zuluaga, R. Pratt, P. A. Patel, M. Aertsen, T. Doel, A. L. David,
34 699 J. Deprest, S. Ourselin, and T. Vercauteren. Interactive medical image segmentation using
35 700 deep learning with image-specific fine-tuning. *CoRR*, abs/1710.04043, 2017.
- 36
37 701 [43] J. Weickert, B. M. Ter Haar Romeny, and M. A. Viergever. Efficient and reliable schemes for
38 702 nonlinear diffusion filtering. *IEEE Transactions on Image Processing*, 7(3):398–410, 1998.
- 39
40 703 [44] J. P. Zhang, Ke Chen, and B. Yu. A 3D multi-grid algorithm for the CV model of variational
41 704 image segmentation. *International Journal of Computer Mathematics*, 89(2):160–189, 2012.
- 42
43 705 [45] Feng Zhao and Xianghua Xie. An overview of interactive medical image segmentation.
44 706 *Annals of the BMVA*, 2013(7):1–22, 2013.
- 45
46 707 [46] W. Zhu, X.-C. Tai, and T. F. Chan. Image segmentation using euler’s elastica as the regular-
47 708 ization. *Journal of Scientific Computing*, 57:414–438, 2013.